Structural and Magnetic properties of colloidal Fe-Pt and Fe cubic nanoparticles

Universität Duisburg-Essen, AG Farle, Experimentalphysik

Michaël Tran

In partial fulfillment of the requirements for the grade

Master of science in *Nanotechnology, Nanomeasurement and Nanocommunication* degree

A thesis presented to the

Institut National des Sciences Appliquées de Toulouse

February - September 2006

Contents

Chapter 1

Acknowledgements

I would like to thank wholeheartedly Prof. Dr. Michael Farle for allowing me to take part in experimental physics in the University of Duisburg-Essen, and for his wise advices on the advancement of my work.

I thank Dr. Marina Spasova, Prof. Dr. Mehmet Acet, Dr. Olivier Margeat (who synthesized all the particles evaluated in this work), Dr. Jochen Kastner, Dr. Jurgen Lindner, Dr. Ralph Meckenstock, Horst Zähres and Michael Venneman for their help, kindness and fruitful discussions all along my work.

I also thank all the other hard working diplom and PhD students: Andrey Lysov, Devendra Chaudhary, Nina Friedenberger, Esperança Manuel, Olga Dmitrieva, Anastasia Trounova, Carolin Antoniak, Oliver Posth, Christopher Hassel...

I thank the students I had in practical work for their patience and comprehension regarding my German language capabilities.

I don't forget the people who contributed to all the wonderful open-source softwares that I used along my work: LaTeX, Open Office, Gimp and Blender.

Chapter 2

Introduction

Organometallics chemistry for the synthesis of nanoparticles is a growing field of interest for both physicists and chemists. It is a very cost effective method that allows to obtain ligands-stabilized nanoparticles in different shapes, different compositions, different structures [1], [2], [3]. In the present work we have investigated the possibilities to synthesize cubic nanoparticles with wet chemistry methods and we have then evaluated their structural and magnetic properties.

Our initial choice to work on the iron platinum alloy was motivated by the fact that it is one of the most promising alloys for magnetic data storage [25] due to properties that will be explained later on in this thesis.

We then continued our researches on iron nanocubes, motivated by the fact that the iron oxide/iron interface should greatly modify the magnetic properties of the nanoparticles.

As a last part of this work, we investigated a new type of ferromagnetic resonance cavities fabricated with lithography techniques. It is one major issue when working with nanoparticles that properties can not be probed individually. Those cavities should allow us to further improve the detection sensitivity of nanoparticles' ferromagnetic and paramagnetic resonance, pushing us closer to single particle resonance.

Chapter 3

Presentation of the University of Duisburg-Essen

The University of Duisburg-Essen is situated in the North-West of Germany, in the region of NordRhein Westfallen (NRW) and more precisely in the ”Ruhr” region which is the most dense of the whole Europe for both its population and industries. The Arbeits Gruppe (working group) of Prof. Dr. Farle is situated in the campus of Duisburg, city which has the largest river port of Europe. It is also known as a miner city since most of the German iron is still extracted here.

The AG Farle does mainly researches on the structure and magnetism of nanoscale Systems: magnetism of small dimensional systems, self-organization, electronic transport, spintronics, magnetotransport. A big effort is aimed towards colloidal nanoparticles, as Prof. Farle is the coordinator of the Marie Curie network ”Synthesis and Orbital Magnetism of Core-Shell Nanoparticles”.

The permanent group itself is formed of:

- Prof. Dr. Farle, specialized in magnetic nanoparticles and ferromagnetic resonance.
- Prof. Dr. Günter Dumpich, specialized in electronic transport.
- Prof. Dr. Mehmet Acet, specialized in materials science and the magnetocaloric effect.
- Dr. Marina Spasova, TEM specialist.
- Dr. Jochen Kästner, responsible for practical work.

Chapter 4

Basics

4.1 Theory

4.1.1 Colloidal nanoparticles

Definition

A colloidal dispersion is a liquid or gel substance which contains particles small enough so that the mixture is homogenous that is when those particles are between 2 nm and 200 nm. Colloidal nanoparticles are wet chemically synthesized (i.e. in solution) particles from metallic precursors and stabilized by capping organic ligands at their surface.

Ligands help avoid coalescence of particles by providing steric repulsion. They allow the particles to be stable in a suspended, non agglomerated state at room temperature. For example, pure iron nanoparticles would be impossible to obtain without capping ligands, because they would oxidize in air in a very exothermic reaction and spontaneously burn. Ligands also allow to control the shape and structure of the particles by controlling the kinetics of their synthesis with parameters such as: temperature, type of ligands and solvent, relative concentration of species, adsorption on preferential surfaces.

The main point to understand is that at the end of the synthesis, the nanoparticles are covered with a layer of organic ligands. Those ligands remain on the nanoparticles even when the particles are taken out of their solvent unless one performs an oxygen plasma on them.

Using chemistry techniques to synthesize nanoparticles is a very promising field because it bears many differences from traditional physical methods such as gas phase preparation [4], laser ablation [5]:

- Preparation at relatively low temperature (between 100^{o}C and 300^{o}C) allows structures different from thermodynamically stable structures at room temperature to be produced.
- The capping ligands also allow nanoparticles with thermodynamically unstable shapes to be synthesized.
- Nanoparticles self-assemble in superlattices when deposited under certain conditions.
- The ligands modify the electronic, magnetic and optical properties of the nanoparticles.

The production of colloidal nanoparticles does not require any UHV nor heavy equipment besides a glove box and the quantity produced can be tuned to industrial amounts, this production method of nanoparticles is also very interesting for industrial applications.

Synthesis theory

The wet synthesis of nanoparticles is based on two main steps which are the nucleation/growth of the metallic clusters followed by their stabilization by organic compounds. As of today the exact theory on the advancement of such reactions is not understood.

Starting from metallic precursors in solution, a basic mechanism theory for the formation of metallic clusters is the burst-nucleation model from Lamer [6] that has been later refined in [7]. This is a two stage growth process in which the solution is first led to supersaturation of metallic atoms by reduction or thermal decomposition of the metallic precursors, leading to nucleation of primary particles. Those primary particles then aggregate through a diffusion controlled process to form bigger, secondary particles depending on chemical conditions in the system.

Stabilization of those metallic clusters is therefore a kinetically driven mechanism since the time elapsed between nucleation and growth steps will determine the size of the final particles. This stabilization is done by coordination bonding between organic ligands and metallic clusters, providing either steric or electrostatic repulsion between the different

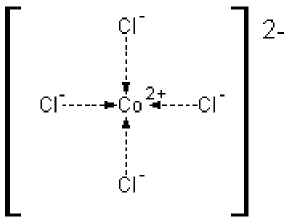

Figure 4.1: Coordination bonds between 4 Cl ions and a Co ion

clusters.

Shape and crystallinity of the nanoparticles also depend on other parameters such as temperature, nature of the solvent in which the reaction takes place, relative concentrations of the many species, etc.

However it is interesting that the thermodynamically stable shape of an isolated single crystalline particle can be determined by the Wulff construction [8] which takes into account the free energies of the surfaces :

$$G = \sum_i \gamma_i A_i \tag{4.1}$$

Where G is the total surface free energy, γ the surface tension and A is the surface, to determine the lowest energy shape. For a typical fcc crystal the thermodynamically stable shape is a truncated octahedron which shape and projection can be seen in Fig 4.1.1.

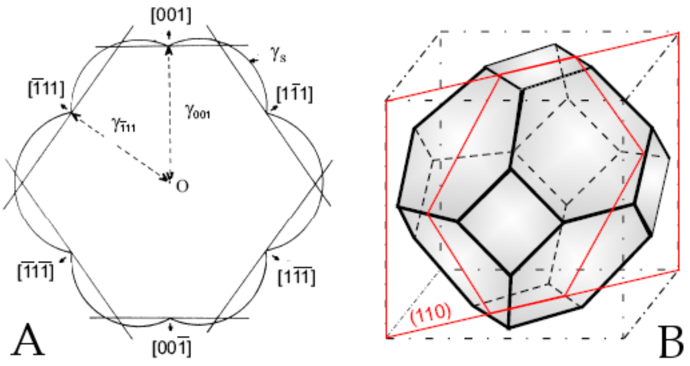

Figure 4.2: (a) Wulff construction of a typical fcc crystal in the plane [110] (b) Schematic of a truncated octahedron, from [9]

4.1.2 Nanomagnetism

It is an experimental fact that ferromagnets can be magnetized more easily along certain crystallographic orientations. The energy difference associated with different directions of magnetization is called the Magnetic Anisotropy Energy.

Magnetocrystalline anisotropy

Magnetocrystalline anisotropy is a consequence of the spin-orbit coupling [15] which can be described by the Russell-Saunders Hamiltonian $H_{LS} = -\lambda \ \overrightarrow{L_i}\overrightarrow{S_i}$: the spin vectors which are responsible for the ferromagnetism feel slightly the anisotropic electrostatic forces which connect the orbital angular momenta of different atoms. For a cubic symmetry (4 fold) the magnetocrystalline anisotropy is written as:

$$F_{MC} = K_0 + K_4(\alpha_x^2\alpha_y^2 + \alpha_y^2\alpha_z^2 + \alpha_z^2\alpha_x^2) + \epsilon \ [erg/cm^3] \tag{4.2}$$

Where the α_i are the direction cosines with respect to the crystallographic axes, K_0 is purely isotropic and K_4 is the 4-fold magnetic anisotropy constant due to the cubic crystallographic symmetry.

For a tetragonal symmetry (2-fold) it can be written as:

$$F_{MC} = K_0 + K_2 sin^2(\theta) + \epsilon \ [erg/cm^3] \tag{4.3}$$

Where K_2 is the 2-fold magnetic anisotropy constant due to the uniaxial symmetry and θ is the angle between the magnetic easy axis and the direction of magnetization.

Dipole-Dipole anisotropy

Dipole-Dipole anisotropy is responsible for the shape anisotropy (demagnetizing field due to the shape of the material) and is given in equation 4.14. It also increases the in-plane anisotropy of a two dimensional array of nanoparticles.

In CGS units it is written:

$$F_{DD} = \frac{1}{2}(N_X M_X^2 + N_Y M_Y^2 + N_Z M_Z^2) \ [erg/cm^3] \tag{4.4}$$

With $\sum N_I = 4\pi$ the ellipsoid of demagnetization factors.

Magnetic anisotropies

A minimum of MAE (i.e. an easy axis of magnetization) can be determined by minimizing the anisotropic part of the free energy density function F which can be expressed in a reduced equation including only anisotropic terms and in the absence of an external magnetic field [32]:

$$F = F_{MC} + F_{DD} + F_{EL} + F_{MAG.EL}\ [J] \tag{4.5}$$

Where F_{MC} is the MagnetoCrystalline magnetic anisotropy energy, F_{DD} is the dipole-dipole anisotropy, F_{EL} is the internal elastic energy and $F_{MAG.EL}$ is the MagnetoElastic anisotropy energy. For the following discussion, let us consider the case of a crystal at constant volume, i.e. only $F_{MC} + F_{DD}$.

The exchange interaction which is responsible for ferromagnetism is not taken into account because this interaction is isotropic[1].

Superparamagnetism

Ferromagnetic materials at the nanometer scale behave differently as "bulk" materials because the magnetostatic energy becomes smaller than thermal energies. Those have therefore increased effects due to size reduction. In the present chapter we will consider single domain nanoparticles.

The magnetic moment of a ferromagnetic nanoparticle is held in one set of directions (uniaxial, cubic, etc.) by magnetic anisotropy energies. Let us consider a spherical particle with uniaxial symmetry for which the shape anisotropy is isotropic (for simplicity). The magnetocrystalline energy is proportional to both the volume and the surface of the particle. The energy barrier due to this energy is described as:

$$\Delta E(B) = K_{eff}(T)V\left(1 - \frac{B}{B_0}\right)\ with\ B_0 = \frac{2K_{eff}}{M_s(T)} \tag{4.6}$$

Where and ΔE is the height of the energy barrier which depends on the applied magnetic field B, K_{eff} is the effective magnetocrystalline anisotropy (depends on temperature [16] taking into account surface and volume anisotropy, V is the volume of the nanopar-

---

[1] The Heisenberg exchange hamiltonian $H_{ij} = -2J^*_{ij}\ \vec{S_i}\vec{S_j}$ is independent of the angles with respect to the crystal axes

ticle and M_s is the spontaneous magnetization that depends on the temperature [17].

As the particle is shrinked, the magnetocrystalline energy diminishes down to the order of the energy barrier between the 2 possible orientations. Depending on the time scale of one experiment, the particle can behave like a paramagnet with a giant susceptibility, or superparamagnet[2].

The switching behaviour between the 2 possible orientations is described by the Neel process:

$$\tau^{-1} = f_0 e^{-\frac{\Delta E(B)}{k_B T}} \tag{4.7}$$

Where f_0 is a frequency factor usually between 10^9 and 10^{12} Hz. This equation defines a time relaxation constant during which the particle's magnetic moment statistically stays in one position. By defining a time scale of 10 - 100 seconds (consistent with SQUID measurements) we can define a blocking temperature:

$$T_B(V) \approx \frac{\Delta E(B)}{30 k_B} \tag{4.8}$$

For $T < T_B$ the particle behaves like a normal ferromagnet, whereas for $T > T_B$ it has a superparamagnetic behaviour.

The name superparamagnet comes from the fact that the magnetic susceptibility of such a particle is equal to: $\chi_{NP} = N \times \chi_{AT}$ where N is the number of atoms in the nanoparticle, χ_{NP} is the susceptibility of the nanoparticle and χ_{AT} the susceptibility of a single atom. In other words, it is giant and can reach orders of 10^5 times bigger as an atomic magnetic susceptibility.

Paramagnetic moment

Without going into details a paramagnetic moment can be described by a Langevin function:

$$\frac{M}{M_s} = coth\left(\frac{\mu B}{k_B T}\right) - \frac{k_B T}{\mu B} \approx \frac{\mu B}{3 k_B T} \tag{4.9}$$

---

[2] All the magnetic moments fluctuate together since they are still ferromagnetically coupled by the exchange interaction

Moreover, considering the small field approximation $\chi << 1$ (contribution from the paramagnetic moments negligible) we can write $B_{total} \approx \mu_0 H$ thus enabling us to find a simple law for the magnetic susceptibility:

$$\chi = \frac{M}{H} \approx \frac{\mu_0 M}{B} = \frac{n\mu_0\mu^2}{3k_B T} \tag{4.10}$$

Where n is the number of paramagnetic moments and μ is the magnetic moment of one atom. It is actually the Curie law.

Temperature dependence of spontaneous ferromagnetic moment

The temperature dependence of the spontaneous ferromagnetic moment can be described by 2 laws depending on the temperature regime:

- At low temperature, the Spin-wave Bloch theory best describes this behaviour:

  $$\mu(T) = \mu_s(T = 0)\left(1 - BT^{\beta}\right) \tag{4.11}$$

  Where $\mu(T)$ is the magnetic moment, μ_s is the saturated magnetic moment (for T = 0 K), B is the Bloch constant and β the Bloch exponent.

- At higher temperature, up to the Curie temperature the Mean-field theory best describes this behaviour:

  $$\mu(T) = \mu_s(T = 0)\left(1 - \frac{T}{T_C}\right)^{\frac{1}{2}} \tag{4.12}$$

  Where T_C is the Curie temperature.

4.1.3 Interactions between particles

Considering a 2 dimensional array of non ionic surfactant-stabilized spherical nanoparticles, we have to take into account 3 interactions to determine the equilibrium force between them. Those interactions are [11] [12]:

- The Van der Waals-London U_{VdW} interaction between 2 spherical particles of diameter D, seperated by a distance r is expressed as:

  $$U_{VdW} = -\frac{A}{6}\left[\frac{2}{\alpha^2 - 4} + \frac{2}{\alpha^2} + ln\left(\frac{\alpha^2 - 4}{\alpha^2}\right)\right] \tag{4.13}$$

Where $\alpha = 2r/D$ and A is the Hamaker constant expressed in Joules. This force increases with increasing particle size.

- The magnetic dipole-dipole interaction U_{dd} between two magnetic dipoles $\vec{\mu_1}$ and $\vec{\mu_2}$ is expressed as:

$$U_{dd} = \frac{\mu_0}{4\pi r^3}\left[\vec{\mu_1} \,.\, \vec{\mu_2} - 3\left(\frac{\vec{\mu_1} \,.\, \vec{r}}{r}\right)\left(\frac{\vec{\mu_2} \,.\, \vec{r}}{r}\right)\right] \tag{4.14}$$

Where $\vec{r}$ is the relative position of the particles.

- The steric repulsion U_{st} between two spherical particles of diameter D with a surfactant shell of thickness δ and density ξ of surfactant molecules per nm^2 on the surface of the particles at temperature T is:

$$\frac{U_{st}}{k_B T} = \left[2 - \frac{l+2}{t} ln\left(\frac{1+t}{1+l/2}\right) - \frac{l}{t}\right] \tag{4.15}$$

where $l = 2s/D$, $s = r - D$ is the separation between surfaces and $t = 2\delta/D$.

4.1.4 Chemical ordering

Considering a metallic alloy with a CuAu structure (like the iron platinum alloy around a composition of 50% iron and 50% platinum), the alloy can exist either in an $A1_0$ "chemically disordered" phase or in a $L1_0$ "chemically ordered" cell.

"Chemically ordered" means that the atoms occupy a specific place in the cell depending on their chemical nature whereas chemically disordered means that the atoms are randomly distributed on the crystal sites. In that latter case, atoms are represented with only one size, since in the whole material, each position bears an average value of each kind of atoms (i.e. all the atoms are shown in the same colour in Fig. 4.3).

Even though $L1_0$ is the thermodynamically stable phase at room temperature (see Fig. 5.1) it is possible to obtain the $A1_0$ phase at room by means of quenching or by synthesizing the alloy by a wet chemical process. Since it is not a stable phase at room

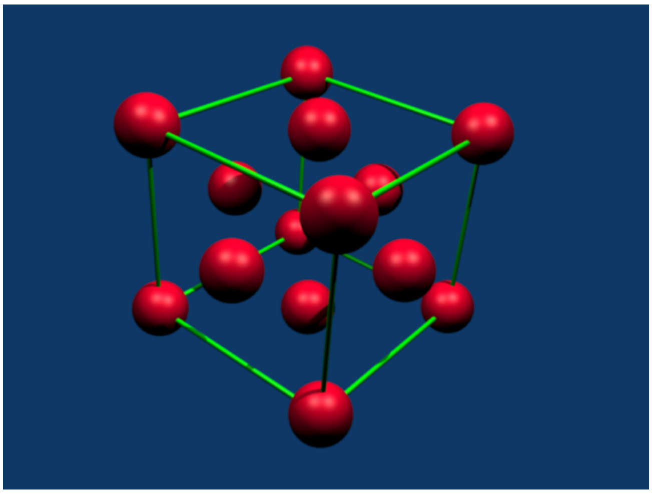

Figure 4.3: $A1_0$ chemically ordered face centered tetragonal basic cell

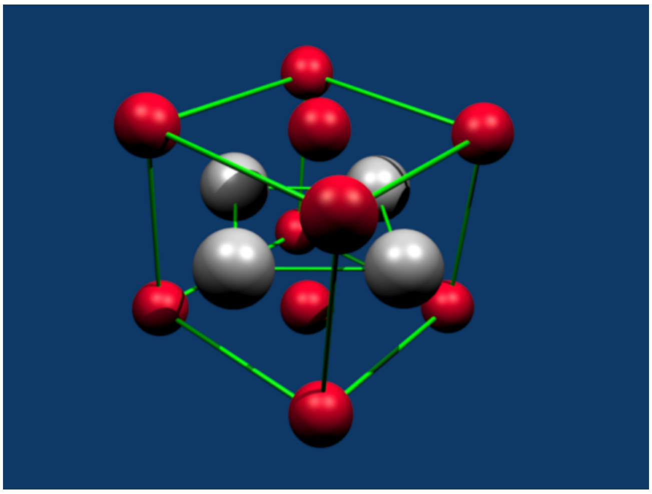

Figure 4.4: $L1_0$ chemically ordered face centered tetragonal basic cell

temperature, it will undergo ordering through a slow diffusion process.

The maximum ordering parameter (which denotes the percentage of ordered cells in a structure) is a function of the temperature as can be seen on Fig. 4.5. It is theoretically maximum at 0 Kelvin and decreases as the temperature approaches the critical temperature above which no more ordering is possible and the stable phase is $A1_0$.

The advancement of the ordering can be described by a TTT (time-temperature-transformation) diagram that gives the time needed at different temperature to increase

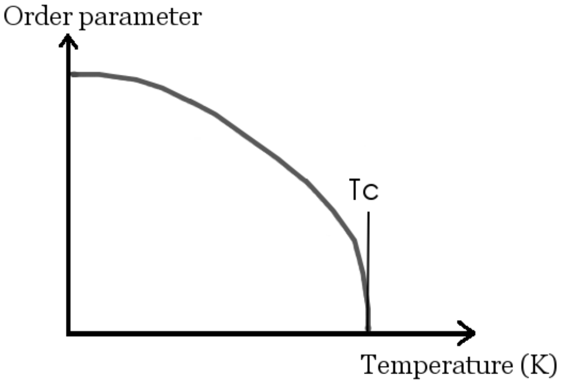

Figure 4.5: Ordering parameter vs temperature

or decrease the order parameter.

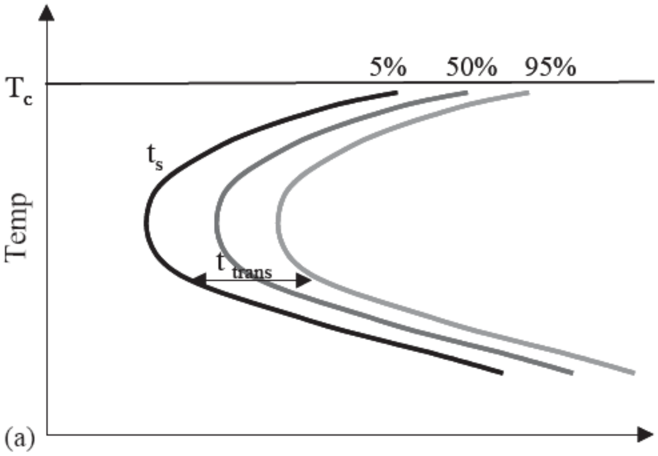

Figure 4.6: Time-temperature-transformation taken from [14]

t_{trans} on Fig. 4.6 is the time required for a transformation from an order parameter of 5% to 95%. The main features of a TTT diagram are as follows:

- Close to the critical temperature T_C the driving force is maximum, the order parameter will be limited to a certain maximum value, as was explained previously.
- At low temperature, the driving force is so small that the order transformation will never happen on an experimental scale.

4.2 Experimental techniques

4.2.1 Imaging with the Transmission Electron Microscope

The Transmission Electron Microscope is a very useful tool for imaging metallic structure which size can be down to some nanometers, the only requirement being that this structure is very thin (less than 50 nm). A very good introduction to the TEM, Electron diffraction and High resolution TEM can be found in the reference [18]. I have been using a Philips CM-12 Transmission Electron Microscope with an accelerating voltage of 120 kV for most of the nanoparticles analysis.

4.2.2 Structural analysis

Electron Diffraction

Determination of quantitative information of a sample in an ED experiment requires a calibration of the TEM with a known sample everytime one takes an ED pattern by exchanging the analyzed grid with a calibration sample (usually gold). Then, using the camera constant equation:

$$\lambda.L = d_{hkl}.R_{hkl} \tag{4.16}$$

λL being the camera constant determined with the calibration sample, R_{hkl} the radius of the considered diffraction ring and d_{hkl} the corresponding interplane distance.

This calibration step is the biggest source of error in this method, since the operator has to change the sample and mechanically bring it to the correct height relatively to the objective lense (eucentric height). This error mainly relies on the skills of the operator but can be estimated at approximately 2% of the measured lattice parameter for a well trained operator. [31]

Xray Diffraction

Xray Diffraction is a very useful and established technique for investigating materials structures: a monochromatic Xray source is directed at the target sample with a certain θ angle. A sensor is placed on the other side of the sample so that it catches the reflected Xrays that satisfy Bragg's law:

$$2.d.sin(\theta) = n.\lambda \tag{4.17}$$

Where d is the interplane distance of the analyzed structure, T the incident angle, n the order of diffraction and λ the wavelength of the incident Xrays.

The device used is a PANalytical X'Pert Pro, equipped with a Copper X-ray tube ($K_{\alpha 1}$ = 1.5405 Å and $Ka_{\alpha 2}$ = 1.5444 Å) and an X'Celerator Real Time Multiple Strip solid-state dector. The acceptance angle of the detector is 0.004^o and is a limiting factor for the resolution of the detector.

Since whole sample is illuminated with Xrays, this method gives averaging results over all the particles on the analysed substrate. One can determine the average crystallite size by analysis of the full width at half maximum of the peaks with Scherrer's equation:

$$CrystalliteSize = \frac{K\lambda}{\Gamma cos(\theta)} \tag{4.18}$$

Where K is the shape factor of the average crystallite, θ the angle of the peak position, λ the wavelength of the incident Xrays and Γ the Full Width at Half Maximum.

High Resolution TEM (HRTEM)

The ultimate and only method of choice when it comes to investigating the structure of single nanoparticles is the High Resolution TEM (HRTEM): no other tool allows one to locally probe the inner structure of materials. It allows through analysis of the pictures using Fourier transformation to measure the interspace distances in all the visible directions for one single crystal and by comparing with crystallographic tables and to determine its structure in the same way Laue diffraction patterns are analyzed. The microscope used for imaging in this work was a Tecnai F20 Supertwin.

4.2.3 Magnetic properties

Ferromagnetic Resonance

Ferromagnetic Resonance (FMR) is a very powerful technique that allows one to probe the magnetic properties. of samples with an energy resolution for magnetic anisotropies on the order of 0.1 μeV [19] with a minimum sensitivity of 10^{11} paramagnetic moments [43]. A good introduction to FMR can be found in the reference [20]. I will simply write the formalism required for the understanding of my results.

By applying an external field B_{ext} to a magnetic sample, the Zeeman interaction:

$$E_{Zee} = m_s g \mu_B B_{ext} \tag{4.19}$$

Where m_s is the spin quantum number, g the Landé factor and μ_B the Bohr magneton. The Zeeman interaction removes the degeneracy of the electrons on a same orbital ($m_s = \pm 1/2$). If a microwave is directed perpendicular to $B_e xt$ at the sample with an energy $E_{\mu w}$ equal to the difference between the two energy levels and this one will be in resonance condition and will be absorbed.

$$E_{\mu w} = h\nu = g\mu_B B_{ext} \tag{4.20}$$

Equation 4.20 is the resonance condition without considering any magnetic anisotropies. It is very interesting since it allows one to determine those magnetic anisotropies by measuring the shift of the resonance field according to the angle of the microwave with respect to the sample. For a thin film the magnetic interaction energy can be written (SI) [21]:

$$\begin{aligned} E \;=\; & -\mu_0 HM - (K_{2\perp} - \frac{1}{2}\mu_0 M^2)\ cos^2(\theta) + K_{2\parallel}\ sin^2(\theta)\ cos^2(\phi - \phi_{2\parallel}) \\ & -\frac{1}{2}\ K_4 \left[cos^4(\theta) + \frac{1}{4}(3 + cos(4\phi))\ sin^4(\theta)\right] \end{aligned} \tag{4.21}$$

In the case of a polar (out of plane) angle along the [100] crystallographic orientation, where M is the magnetization of the sample and H the applied field. In the case of nanoparticles it is possible to use this equation in first approximation by adding a filling factor f to the $(1/2)\mu_0 M^2$ shape anisotropy term that becomes $(1/2)f\mu_0 M^2$ as long as the array of nanoparticles is textured along the (100) axis.

By solving the Landau-Lifshitz-Gilbert equation, the resonance frequency ω is then written:

$$\left(\frac{\omega}{\gamma}\right)^2 = \frac{1}{M^2}\left[E_{\theta\theta}\left(\frac{E_{\phi\phi}}{sin^2(\theta)} + \frac{cos(\theta)}{sin(\theta)}E_\theta\right) - \left(\frac{E_{\theta\phi}}{sin(\theta)} + \frac{cos(\theta)}{sin(\theta)}\frac{E_\phi}{sin(\theta)}\right)^2\right] \tag{4.22}$$

Where E_x and E_{xy} are the 1^{st} resp. the 2^{nd} order derivatives of the energy with respect to the angles and γ is the magneto-mechanical ratio for an electron spin.

FMR thus allows one, by measuring:

- The angular dependence of the resonance field, to determine the magnetic anisotropies.
- The intensity of the resonance field at different microwave frequencies or in a powdersample to determine the Landé g factor.
- The absorption intensity to determine the magnetization of the sample.

SQUID

The Superconductin Quantum Interference Device combines the physical phenomena of flux quantization and Josephson tunneling to detect tiny changes in an applied magnetic flux. It is basically a flux to voltage converter and allows to measure magnetic fields on the order of the femtotesla. A good introduction to SQUID can be found in ref [22].

Chapter 5

Iron-Platinum nanocubes ($FePt_3$)

Iron platinum alloy might be used as material for magnetic storage media. This is however not the only reason: the binary alloy formed of Iron and Platinum is very rich in terms of diversity of magnetic properties. Three main phases can be observed depending on the concentration and temperature of the alloy:

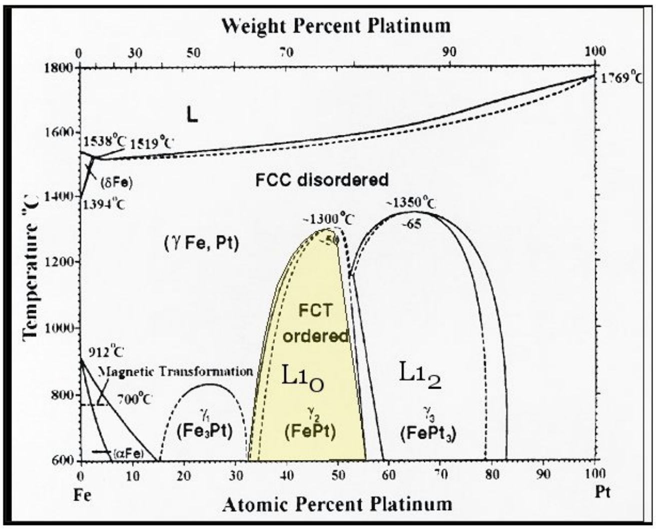

Figure 5.1: Phase diagram of the Iron Platinum alloy

- Fe_3Pt which has an Invar property in its disordered form when the relative concentration of Iron is higher than 75% [23].
- FePt which has the highest magnetic anisotropy energy of all the transition metal alloys ($7.10^6 J.m^{-3}$) when in its $L1_0$ phase along with a uniaxial symmetry along the

c axis due to a Face Centered Tetragonal (or Face Centered Cubic Distorted). This phase could be used for magnetic storage.

Fig. $L1_0$ phase structure

- $FePt_3$ which is ferromagnetic in its disordered phase, has two antiferromagnetic ordering in its $L1_2$ phase ($CuAu_3$ structure) and is a very interesting alloy to study the effect of induced magnetization on Platinum atoms by Iron neighbours.

  Fig. $L1_2$ phase structure

Therefore, the initial idea was to obtain nanomagnets of iron platinum in its $L1_0$ phase. For this purpose many hurdles would need to be overcome. One of them is the obtention of nanoparticles with the correct crystallographic structure in order for the magnets to have a blocking temperature on a large time scale (more than 10 years) situated above room temperature so that the information would not be lost. This first step requires particles with a concentration of the alloy around $Fe_{50}Pt_{50}$ and possibly further annealing as will be explained in section 5.1.1 page 23.

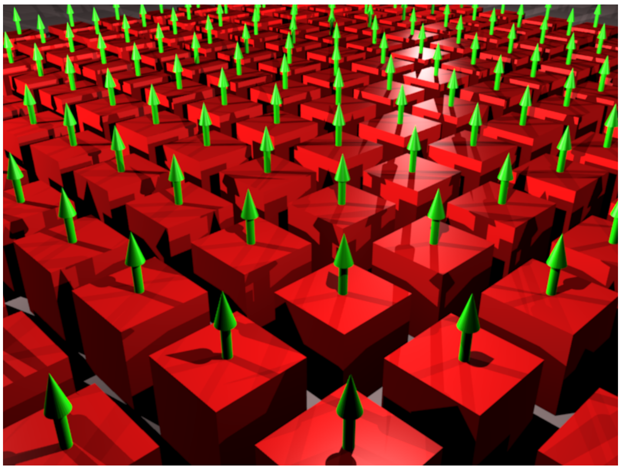

Figure 5.2: Array of particles with all directions of magnetization aligned

Another problem is the necessity to have all magnetic moments of the particles aligned parallel one to each other. This means we need to deposit the particles on a substrate with a clearly definite direction of the particles' magnetic moments, which is not the case with usual spherical nanoparticles. One idea is to engineer cubic nanoparticles which distorted c axis would be perpendicular to the substrate.

Nanocubes which facets would be along the basic crystallographic orientations i.e. [100], [010] and [001] would constitute a first advancement towards a possible application as magnetic storage (see Fig. 5.2).

This requires a solid knowledge of the mechanisms of growth of nanoparticles during wet synthesis. The problems are: first that cubic shapes are anything but natural and then, that those surfaces we would like to have as facets are not as dense as (111) and therefore not thermodynamically stable in normal conditions[1]. In this work we have explored the the addition of capping ligands using wet chemistry methods as a way to synthesize and stabilize Iron Platinum nanocubes.

5.1 Synthesis of Iron Platinum cubes

5.1.1 A long road to the synthesis of nanocubes

Starting point

The synthesis that has become a standard for iron platinum nanoparticles was published by Sun et al. [25] and consists of a simultaneous reduction of a Platinum salt $Pt(acac)_2$ by a diol Hexadecanediol and the thermal decomposition of an iron precursor $Fe(CO)_5$ in the presence of two ligands: oleic acid and oleylamine.

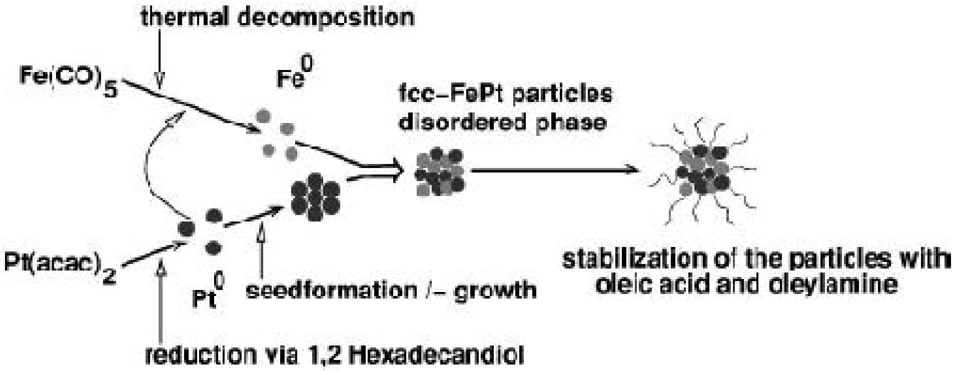

Figure 5.3: Synthesis of FePt nanoparticles taken from [24]

---

[1] The surface energy is proportional to the number of dangling bonds. As a general rule of thumb, the more dense the surface, the smaller the number of dangling bonds, the lower the surface energy.

A typical synthetic procedure is as follows [25]: in inert atmosphere, $Pt(acac)_2$ (0.5 mmol), Hexadecanediol (1.5 mmol) and Dioctylether (20 mL, solvent) are mixed and heated up to 100°C. Oleic acid (0.5 mmol), Oleylamine (0.5 mmol) and $Fe(CO)_5$ (1 mmol) are then added and the mixture is heated to reflux at 297°C for 30 minutes. The particles are then precipitated by addition of ethanol, redispersed in Heptane and centrifugated to isolate and purify them.

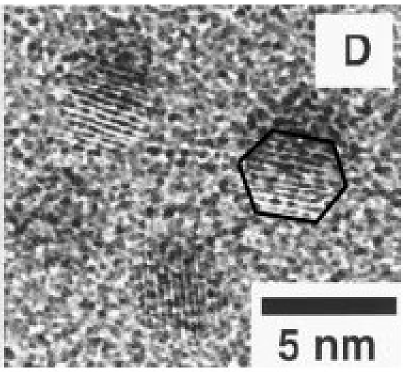

Figure 5.4: TEM image of as prepared particles synthesized as stated above taken from [25]

The particle size can be tuned from a diameter of 3 to 10 nm by first growing 3-nm monodisperse seed particles in situ and then adding more reagents to enlarge the existing seeds to the desired size. The particles are actually not spherical but have definite surface planes as can be seen on Fig 5.4 where the contour of a particle has been highlighted by software. If the particles effectively grow along crystallographic directions then it should be possible to modify the chemical environment during the synthesis in order to decrease the free energy of specified surfaces. Therefore choosing the growth crystallographic directions (see 4.1.1 page 9).

The internal crystallographic structure of these particles is found to be face centered cubic (fcc) disordered which corresponds to a thermodynamically unstable phase at RT (see Fig. 5.1). This structure is due to the fact that the formation of nanoparticles is a diffusion process. Therefore, synthesizing at a temperature under 300°C does not allow the atoms to have a sufficient energy to to overcome the activation energy barrier in an experimental time scale (see 5.6 page 43. Unfortunately for applications, the interesting structure for FePt nanoparticles is the $L1_0$ ordered phase which can only be obtained by further annealing.

Influence of synthesis parameters

Starting from the current knowledge on FePt nanoparticles wet synthesis [25], [26], [27], [28] we started investigating the different parameters influencing the results of the synthesis:

- *Type of solvent*:
    - Dioctylether: Leads to spherical particles at 280°C and star-shaped particles at 170°C. This solvent was used at first in the synthesis by Sun et al. [25].
    - Mesitylene: Leads to star-shaped particles. This solvent is apolar.
    - Dichlorobenzene: Leads to cubic particles. This solvent is polar and has a Cl atom.

  One other parameter to take into account is that the amount of water still in the solvents after distillation is different from one to another and this can also influence the chemical reactions.
- *Temperature*: Using the synthesis procedure for $FePt_3$ nanocubes and varying the temperature we obtain:
    - At 130°C: Star-shaped particles
    - At 170°C: Cubes
    - At 230°C: Cubes with round edges mixed with spherical particles
    - At 280°C: Spherical particles
- *Duration of the synthesis*: Using the synthesis procedure for $FePt_3$ nanocubes and stopping the reaction at different times:
    - 5 min: Spherical particles
    - 20 min: Some cubes with round edges and mostly spherical particles
    - 1 hour: Same results with increased number of cubes
    - 12 hours: Cubic particles

- *Relative concentrations of ligands*: Using the synthesis procedure for $FePt_3$ nanocubes with different ligands concentrations[2]:
  - (1:1) Leads to polydisperse spherical particles
  - (1:8) A large excess of ligands leads to cubic particles
- *Relative concentrations of precursors*: Using the synthesis procedure for $FePt_3$ nanocubes with different relative precursors concentrations[3]:
  - (3:2) Cubes with a concentration around $Fe_{30}Pt_{70}$
  - (2:1) Cubes with a concentration around $Fe_{30}Pt_{70}$
  - (4:1) Mix of cubes with a concentration around $Fe_{30}Pt_{70}$ and two-bodies cubic particles in which a segregation of iron and platinum is observed
  - (8:1) Mostly two-bodies cubic particles
- *Ramping of temperature*: This parameter did not seem to influence the obtention of nanocubes.

These parameters are of course not independent and it would take more than a PhD thesis to discover all the mechanisms of synthesis.

For each synthesis the particles have been deposited on copper grids covered with an amorphous carbon film. Morphology has been observed in bright field TEM, chemical composition with Energy Dispersive X-Ray Spectroscopy (EDX) and crystallographic structure by Electron Diffraction in a Philips CM-12 TEM.

5.1.2 Synthesis of $FePt_3$ nanocubes

A recent publication from Nisha Shukla [29] shows a successful wet synthesis of FePt nanocubes. The author claims that the particles are single crystalline with cubic shapes and that they organize of surfaces with local order and a square superlattice. More importantly, they orient themselves with their [100] axis perpendicular to the surface.

---

[2] (i:v) means a ratio of i equivalents [$Fe(CO)_5$ + $Pt(acac)_2$] to v equivalents [Oleylamine + Oleic acid]

[3] (i:v) means a ratio of i equivalents [$Fe(CO)_5$] to v equivalents [$Pt(acac)_2$]

The synthesis procedure for these nanocubes is as follows. In inert atmosphere Fe(CO)$_5$ (0.5 mmol), Pt(acac)$_2$ (0.5 mmol), Oleic acid (4 mmol), Oleylamine (4 mmol) are diluted in Dichlorobenzene (solvent). The mixture is heated up to a reflux temperature of 170^{o}C at a rate of 4^{o}C per minute. A standard washing procedure is then applied to remove the smallest particles and remove the excess of ligands.

Since the article does not make any statement on structural and magnetic properties (no information on the composition, no magnetic measurement) of these FePt nanocubes, we reproduced the synthesis procedure in our laboratory in order to investigate those properties.

Reproduction of the synthesis was done in our laboratory using the procedure by Shukla described above but with Hexadecylamine (HDA) replacing Oleylamine and by heating directly at 170^o. The reason for using HDA instead of Oleylamine is that the product is available in 99.9% pure solutions which is not the case for Oleylamine.

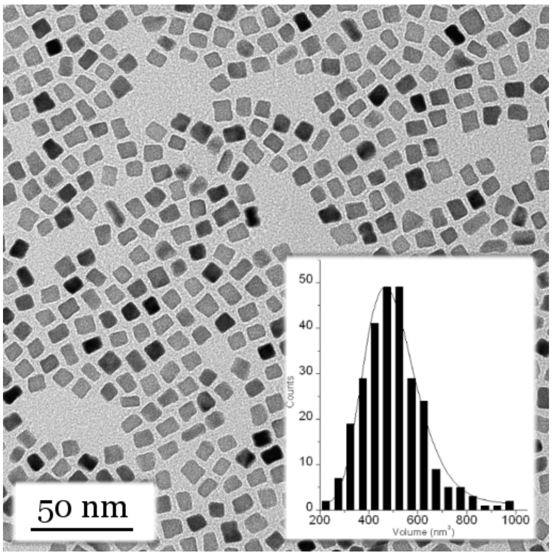

Figure 5.5: Overview and Volume distribution of as synthesized FePt$_3$ nanocubes

The nanocubes obtained from the synthesis are very similar to the the particles described by Shukla, as can be seen on Fig. 5.5. The nanocubes have a most probable edge length of 7.88 nm and their volume (but also length) follows a log-normal distribution with a mean volume $<V> = 502.07$ nm^3 and a dispersion s = 0.221 nm^3 assuming an average value of cubes' lengths to calculate the volume. See inset of Fig. 4.5. These calculations

Number	Fe (%)	Pt (%)	σ (%)	Number	Fe (%)	Pt (%)	σ (%)
1	32.28	67.72	1.96	15	29.17	70.83	1.77
2	30.59	69.41	2.19	16	27.05	72.95	0.99
3	32.75	67.25	1.51	17	26.66	73.34	1.39
6	31.4	68.6	2.18	21	29.76	70.24	2.02
8	26.28	73.72	1.86	24	32.82	67.18	2.13
9	27.57	72.43	1.81	25	29.45	70.55	2.11
10	27.98	72.02	1.61	26	26.51	73.49	1.98
11	29.97	70.03	1.94	27	30.65	69.35	2.28
12	34.62	65.38	2.67	28	26.02	73.98	1.78
13	28.1	71.9	1.87	29	30.34	69.66	2.62
14	28.14	71.86	1.65	30	23.93	76.07	1.9

Table 5.1: Analysis of the $FePt_3$ nanocubes by nanoprobe EDX

have been made according to TEM pictures, which means that they don't take into account the thickness of the ligands which are too light elements to be imaged by electrons at magnifications > 20000.

Energy Dispersive Xray (EDX) spectroscopy using the TEM nanoprobe mode with a beam size of 10 nm allows us to determine the composition of nanocubes in local areas (between 5 and 10 nanocubes analysed each time). Results given in table 5.1 show a relative mean composition of the particles of 29.18% Iron and 70.82% Platinum with a standard deviation $s = 2.64$ %. This deviation value is very small compared to usual synthesizing methods using $Fe(CO)_5$ as a precursor as can be read in [13].

The nanocubes are in the $FePt_3$ structure composition range as can be seen on Fig 5.1. It is however clear that the composition value determined has no statistical meaning since the analysis should have been done on at least 300 nanocubes to approach the expected value, which value could be as far as ± 5% from the currently determined composition.

5.2 Structural properties

Fig. 5.6 shows a high resolution electron micrograph of a single $FePt_3$ nanocube taken with a Tecnai F20 Supertwin. Analysis by Fourier transformation allows us to index the spatial frequencies of the cube and compare them with known tables of usual structures. From the phase diagram, Iron-platinum alloy should have a face cubic centered structure in all of its possible structures except for the $L1_0$ phase.

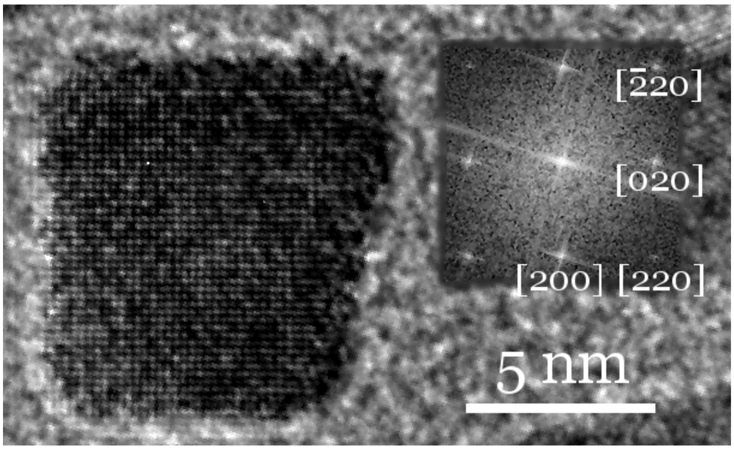

Figure 5.6: High Resolution Pictogram of an $FePt_3$ nanocube as prepared and Fourier transformation as inset

Analysis of the angles between the family planes of the nanocubes and their lengths for 15 different nanocubes of a same sample allows to confirm the fcc structure and determine the crystallographic orientations (see inset of Fig 5.6). The absence of forbidden fcc reflections confirms that the as prepared nanocubes are in the fcc disordered structure.

All the nanocubes analyzed were single crystals with a mean lattice parameter of a = 4.02 Å with a standard deviation s = 0.03 Å. Litterature value for the lattice parameter of bulk $Fe_{30}Pt_{70}$ (30% of Iron and 70% of Platinum) is a = 3.87 Å [23] which gives a lattice expansion of 3.9% for the nanocubes. It is however a known issue that high resolution electron micrographs can give rise to errors as big as 10% when measuring metal nanoparticles lattice parameters, because of a relaxation of the Bragg condition [30].

Therefore, ED and XRD has been performed on the $FePt_3$ nanocubes in order to determine the lattice parameter with other methods.

The sample for XRD has been prepared by first cleaning a 4 mm × 4 mm (100) silicon wafer with acetone during 10 minutes in ultrasounds. A drop of the nanocubes' solution was then dropped using a pipette on the substrate and was allowed to evaporate for 1 hour. This step was repeated until a clear black spot became visible to the unaided eye after drying. Ligands deposited on the side of the substrate ("Coffee rings") were carefully removed using a scalpel.

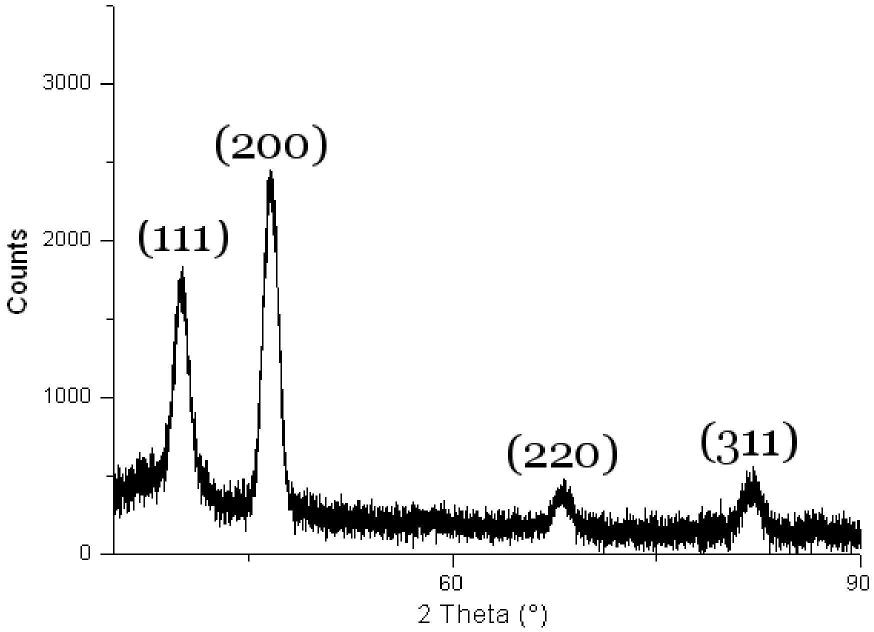

Figure 5.7: XRD spectrum of as prepared $FePt_3$ nanocubes

The XRD spectrum (Fig 5.7) shows a (200) peak that has an intensity higher than the (111) peak. According to the powder diffraction simulation done with Carine Crystallography (Fig 5.8) for an fcc structure with a lattice parameter a = 3.87 Å corresponding to the bulk value for $Fe_{30}Pt_{70}$, the intensity of the (111) peak should be twice as the intensity of the (200) peak. This is a clear evidence of a strong (100) texture. Lattice parameter determined by analysis of the angles of the (111), (200), (220) and (311) peaks is a = 3.893 Å ± 0.005 Å.

Electron Diffraction has also been performed on a normal TEM copper grid. Calibration of the camera constant has been done by exchanging the $FePt_3$ sample with a gold thin film on a copper grid which diffraction peaks are known. The value determined by measurement of the eight first diffraction rings was a = 3.86 Å ± 0.07 Å [31] with a stan-

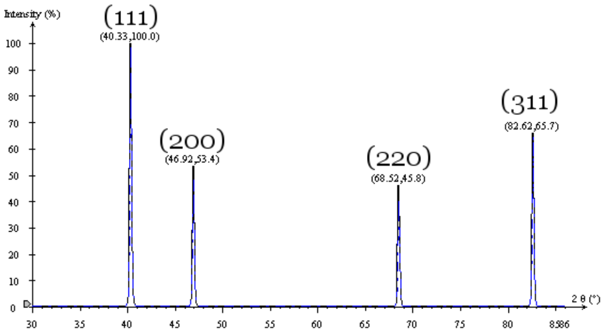

Figure 5.8: Powder diffractogram simulated for an fcc structure with bulk like lattice parameter of $FePt_3$

dard deviation s = 0.006 Å.

5.3 Texture

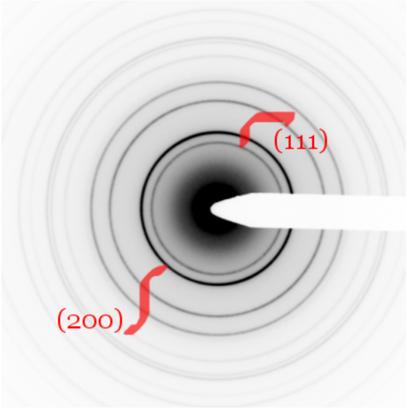

Figure 5.9: MO52 Electron Diffraction tilted @ 0^o

Texture of the particles' assembly is evidenced by electron diffraction. Fig 5.9 resp. Fig 5.10 show an electron diffractogram (colours are inversed for a better display) with the sample perpendicular resp. tilted at 45^o from the electron beam (precision of the goniometer here is not an issue). For an fcc structure powder diffraction diagram, the (111) ring always has the highest intensity whereas here at 0^o it is clear that the (200) reflection is more intense than the (111). Since the intensity of a given reflection (h, k, l) is proportional to the number of h, k, l planes in reflecting condition (Bragg's law) it is a first evidence of

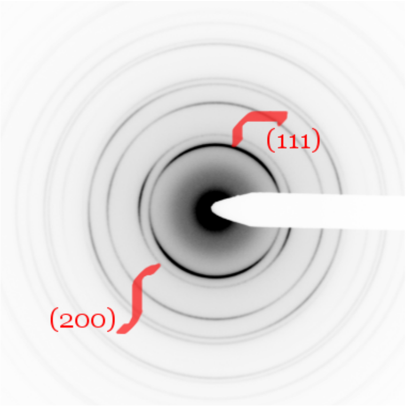

Figure 5.10: MO52 Electron Diffraction tilted @ 45^o

a strong (100) texture.

Tilting at 45^o increases the intensity of the (111) ring while decreasing the intensity of the (200) ring, both in a non homogeneous way:

- The increase in intensity of the (111) is due to a strong (100) texture in the plane: the angle between (111) and (100) is 54.73^o, so tilting 45^o brings the (111) planes closer to the Bragg condition.
- Non homogeneity of the rings: in the case of a fiber-like texture, the reciprocal lattice nodes form a non-uniform sphere in the reciprocal lattice (as opposed to a uniform sphere in the case of an ideal randomly-distributed polycrystalline sample). Therefore the intersection of the Ewald sphere, approximated to a plane in the case of electron diffraction, with the lattice nodes will result in inhomogeneities depending on the angle between the texture axis and the Ewald plane [34] [35].

The strong (100) out of plane texture is therefore evidenced by electron diffraction and also confirmed by the previous XRD measurements (Fig. 5.7).

5.4 Annealing

In-situ annealing of the nanocubes in the TEM has been done for two purposes:

- Confirm our assumption that the particles effectively possess the FePt$_3$ structure.

- Study the agregation process of the nanocubes at high temperature.

The sample was prepared by dropping the nanocubes' solution onto a nickel TEM grid covered with an amorphous silicon oxide (SiO_2) layer. A first anneal up to 400°C was done in a vibrating sample magnetometer in 900 mbar ± 30 mbar of helium atmosphere during one hour. This avoids the thermal decomposition of the ligands (that occurs at around 300°C) in vacuum which would lead to their evaporation and would leave the nanocubes unprotected against agregation.

5.4.1 $L1_2$ phase

If the as-prepared fcc disordered structure orders into the chemically ordered $L1_2$ phase when annealing temperatures above 600°C, $FePt_3$ structure will be confirmed. A simple way to determine the $L1_2$ chemical ordering of the nanoparticles is to observe the apparition of new rings in a diffraction pictogram.

For a common fcc structure with randomly organized atoms the atomic diffusion factor is averaged over the diffrent atoms and the structure factor F_K is given (If $F_K = 0$ for one (h k l) plane, then the reflection is forbidden):

$$F_K = f \times [1 + e^{-i.\pi.(h+k)} + e^{-i.\pi.(k+l)} + exp^{-i.\pi.(h+l)}]$$

f the average atomic diffusion factor of the atoms
h, k, l the indices of the reflections.

Whereas for a chemically ordered structure the atomic diffusion factor is specific to each atomic position:

$$F_K = f_1 + f_2 \times e^{-i.\pi.(h+k)} + f_3 \times e^{-i.\pi.(k+l)} + f_4 \times e^{-i.\pi.(h+l)}$$

f_i the atomic diffusion factor of the i^{th} atom

We clearly see that in the case of a chemical ordering, suppressed reflections because of the fcc structure will be allowed due to differences in atomic electron densities. The rings already present in the fcc disordered structure must remain unchanged because no lattice

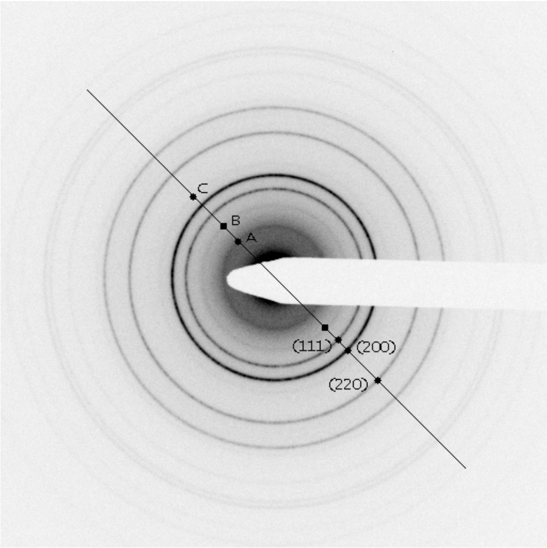

Figure 5.11: Electron Diffraction pattern after annealing @ 700^{o}C Tilt 0^o

expansion is involved during the ordering transformation.

Fig. 5.11 shows an electron diffraction pattern taken at 700^{o}C after 2 hours and 30 minutes of annealing in-situ. Rings that were already present before annealing (Fig. 5.9) are written (111), (200) and (220). New rings have been written as A, B and C. Ratio comparison of ring diameters allows to determine them to be: A = (100), B = (110) and C = (210) which is consistent with the L1$_2$ phase without ambiguity and confirms our asumption based on the composition of the nanocubes.

Moreover, it is clear from the intensity of the (200) diffraction ring that the (100) texture is still strong even after annealing for more than 2 hours at 700^{o}C.

One other aspect observed during the experiment is that the chemical ordering process is time dependent. At a constant temperature, the intensity of the superlattice reflections were growing as time was passing. This is consistent with the fact that chemical ordering is a diffusion process.

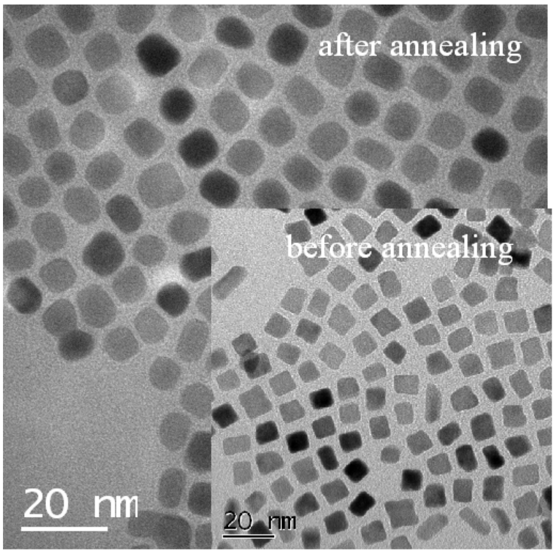

Figure 5.12: TEM images before and after annealing of $FePt_3$ nanocubes

5.4.2 Shape evolution and agregation process

Fig. 5.12 shows a TEM picture of $FePt_3$ before and after annealing up to 400^{o}C. The nanoparticles roughly keep their cubic shape, but the edges of the cubes become rounder. The shape of the nanoparticles does not change dramatically after annealing at higher temperatures, but a process of agregation occurs.

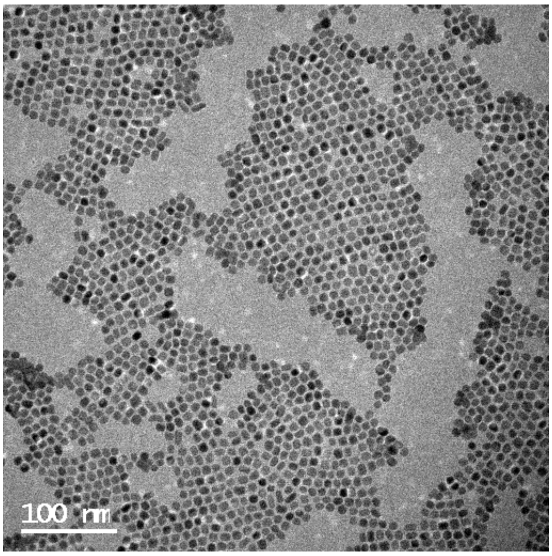

Figure 5.13: TEM picture of $FePt_3$ nanocubes at 400^{o}C

Agregation of colloidal nanoparticles during annealing is one current major issue. In the case of iron platinum alloys, it prevents one to obtain chemically ordered phases ($L1_0$ or $L1_2$ depending on the composition) with well shaped nanoparticles. It is therefore useful to understand how this process occurs.

While annealing in-situ, a series of electron micrographs has been taken in order to try and determine key points of this process.

Fig. 5.13 shows an electron micrograph taken at 400°C after annealing in helium atmosphere.[4] The particles are mostly not agregated except for some situated on the borders of assembled areas.

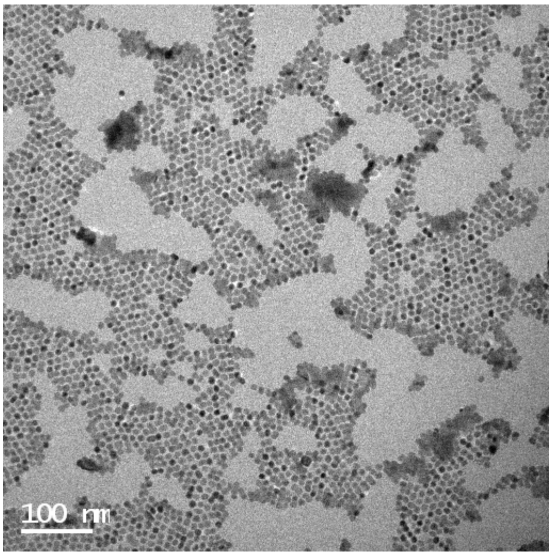

Figure 5.14: TEM picture of $FePt_3$ nanocubes at 575°C

Fig. 5.14 is an electron micrograph taken at 575°C. The agregation is clearly more severe than after annealing at 400° and a rough estimation of 10% of agregated particles can be done. Again, the particles situated on the borders of assembled areas are subject to heavy agregation, while particles situated inside these assembled areas do not seem to suffer from agregation. From the observations done during the experiment those conclusions can be

---

[4] The white spots correspond to reflections of the incident electron beam due to the crystalline structure of the particles. They can be removed by use of an objective aperture in TEM, but the contrast was too bad to use it here.

drawn:

- The longer the annealing at a constant temperature, the more the agregated particles. Agregation is a time dependent process.

- The agregation process highly depends on the way the sample is prepared. Particles within a nicely organized sample will be less agregated than particles without organization in the same time and temperature conditions.

- When looking at a single place with the TEM, very few agregation occurred under the beam.

5.5 Magnetic properties

5.5.1 Curie temperature and magnetic moment

SQUID magnetization measurements have been performed on the $FePt_3$ nanocubes: as prepared solution was precipitated by addition of ethanol and dried under inert argon atmosphere. Resultant 9 mg powder were enclosed in a special SQUID diamagnetic capsule. Magnetic contribution from the capsule was separately measured and substracted from shown data.

Fig 5.5.1 shows experimental data acquired at zero applied field from 0^+ K to Curie temperature. The presence of a spontaneous magnetic moment confirms our asumption that the nanocubes are ferromagnetic and with a Curie temperature below room temperature.

Fitting the low-temperature regime of the curve with the Bloch theory (equation 4.11) results in parameters:

$$M(T) = 4 \times 10^5 \left[1 - 9 \times 10^{-4} T^{1.12}\right]$$

Considering that all 9 mg of powder are nanoparticles and that the density of $Fe_{30}Pt_{70}$ is $d = 18.36\ g.cm^{-3}$. This gives a value for the saturation magnetization $M_s = 400$ kA/m

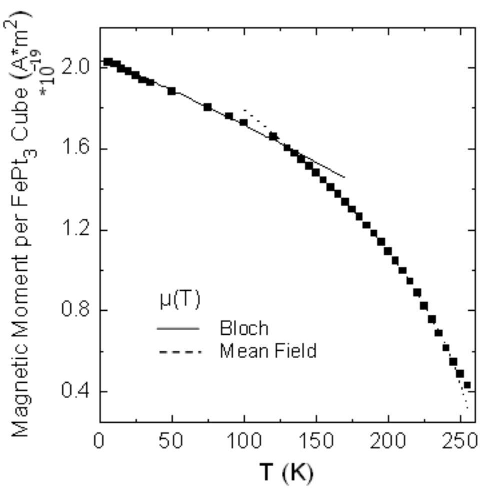

Figure 5.15: Magnetic moment versus Temperature of $FePt_3$ nanocubes

and a magnetic moment of a single nanocube $\mu_p = 2.03 \times 10^{-19}\ A.m^2$ which corresponds to a magnetic moment per $FePt_3$ unit cell of $\mu_{cell} = 2.53\ \mu_B$.

Fitting the temperature regime closer to the Curie temperature with the mean-field theory (equation 4.12), a $T_C \approx 255$ K is found.

5.5.2 Field Cooled / Zero Field Cooled experiment

The temperature dependence of the initial magnetic susceptibility was measured by rising the temperature from 5 K to 370 K after cooling the sample in a zero magnetic field (ZFC) and after cooling in a magnetic field of 2 mT (FC). ZFC and FC susceptibilities show a typical behaviour for an assembly of superparamagnetic particles: the FC susceptibility decreases while the ZFC susceptibility increases with rising temperature and reaches a maximum at $T \approx 104$ K, that is the blocking temperature T_B[5]. Then the susceptibility decreases as the temperature increases.

For a ferromagnet the susceptibility is usually described by a Curie-Weiss law

$$\chi(T) = \frac{C}{T - T_C}$$

---

[5] Normally T_B should be determined by fitting the curve with a magnetic moment distribution weighted equation, but since the ZFC measurements around T_B are quite symmetric, simply choosing the maximum χ as T_B is quite correct.

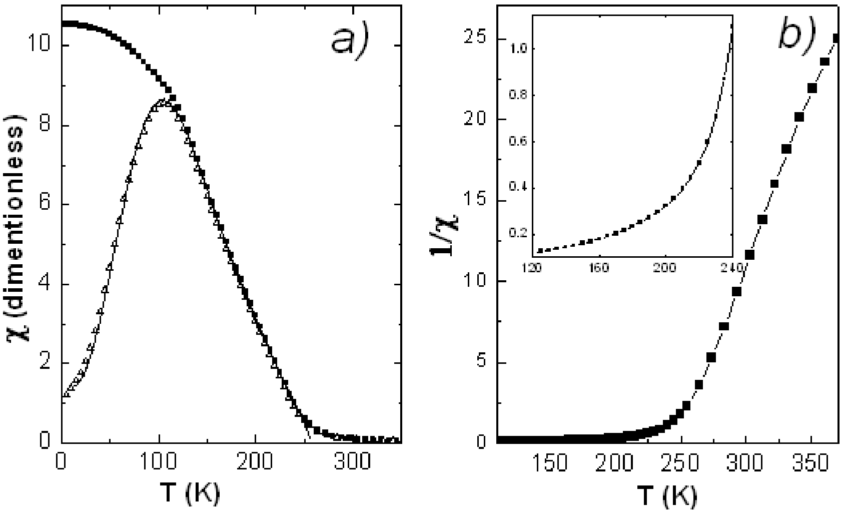

Figure 5.16: (*a*) Temperature dependence of Field Cooled/Zero Field Cooled susceptibility (*b*) Inverse susceptibility versus temperature above the blocking temperature, with a zoom on the superparamagnetic regime as inset

With C the Curie constant. However if we take a look at Fig. 5.5.2 (*b*) it is clear that $1/\chi$ is not linear versus T in the superparamagnetic regime ($\sim$ 104 - 255 K) whereas it is linear in the paramagnetic regime (T $>$ 255 K). This can be explained by the following reasoning:

- By writing the Curie constant for a superparamagnetic moment (the moment of each nanocube has to be considered instead of the atomic moment)

  $$C = \frac{\eta \mu_0 \mu_p^2(T)}{3k_B}$$

  Where η is the number of superparamagnetic moments per unit volume and μ_p is the average magnetic moment of a single nanocube.

- The behaviour of the low-field susceptibility is then described by a Curie-Weiss-like law [33]

  $$\chi(T) = \frac{\eta \mu_0 \mu_p^2(T)}{3k_B(T + T^*)}$$

  Where T^* is a temperature which represents the effect of long-range dipolar magnetic interaction between the nanoparticles.

- One can also write the energetic contribution of the dipolar interaction as

  $$k_B T^* = \epsilon_D = \frac{\mu_0}{4\pi} \frac{\alpha \mu_p^2(T)}{d^3}$$

  Where α is a constant derived from the sum of all dipolar interactions among the particles and d is an average distance between the neighbouring dipoles.

- Moreover the magnetic moment of a particle can be written in the temperature regime near T_C according to the mean field theory

  $$\mu_p(T) = \mu_p(0) \left(1 - \frac{T}{T_C}\right)^{\frac{1}{2}}$$

- The inverse susceptibility can therefore be written

  $$\frac{1}{\chi} = \frac{3k_B T_C}{\eta \mu_0 \mu_p^2(0)} + \frac{T}{(T_C - T)} \frac{3\alpha}{4\pi \eta d^3}$$

  Which is clearly not linear with T.

One could continue this analysis to quantitatively determine K_{eff} and the dipolar interaction energy of the particles [17] but with our currently available data it would lead to many speculations.

5.5.3 Landé factor

The sample for the EPR spectrometer of $FePt_3$ nanocubes was prepared by first precipitating the nanocubes by adding ethanol to the solution. The obtained powder was then dryed in Argon atmosphere and inserted in a gelatine capsule which was directly used for EPR measurements. The experiment was conducted in an X-band cavity with an oscillating field at *9.853 GHz*.

Since the Curie temperature is ~255 K, the nanocubes should be in paramagnetic regime at room temperature. This means that the magnetic anisotropies all vanish [32] and that a single EPR measurement on powder will reveal enough information to calculate the Landé (g) factor of the nanocubes.

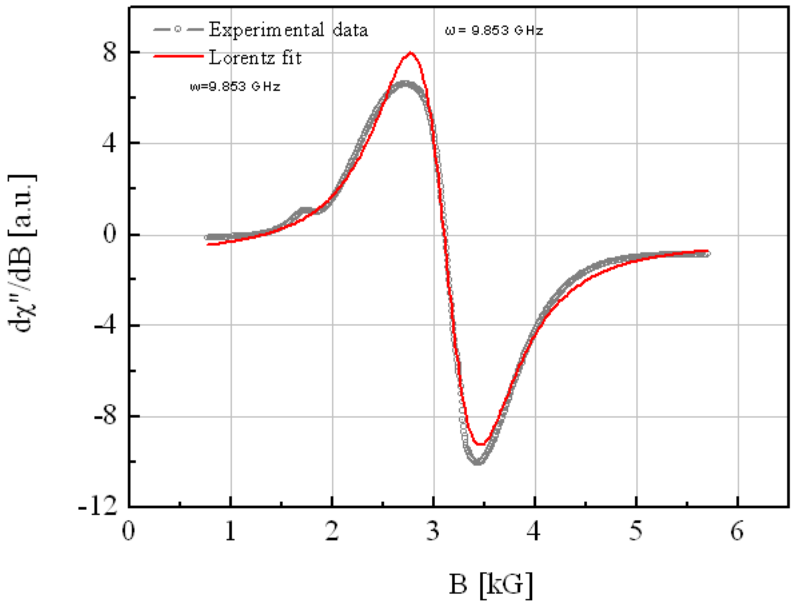

Figure 5.17: Powder FMR spectrum of FePt$_3$ nanocubes

Fitting the EPR signal (Fig. 5.17) with a single derivate of a Lorentzian line allows us to determine the resonance field of this sample at $H_0 = 313\ mT \pm 3\ mT$. From the resonance condition given in [10] we find that:

$$g = \frac{h\nu}{\mu_B B} = 2.25$$

The error can be estimated from the precision on the resonance field and the microwave frequency ($\Delta\nu \approx\ 0.005GHz$):

$$\Delta g = \frac{h}{\mu_B B} \times \Delta\nu + \frac{h\nu}{\mu_B B^2} \times \Delta B = 0.02$$

As a final result, we obtain $g = 2.25 \pm 0.02$ for the FePt$_3$ nanocubes.

5.6 Further discussions

Obtention of nanocubes

The exact mechanisms of growth leading to cubic nanoparticles are still unknown. However as a rule of thumb we can expect one of the chemicals in reaction (probably the solvent, as has been demonstrated by Shukla et al. in [29]) to have surface-specific interactions with the metallic seeds, reducing their surface energy by forming links with the dangling bonds. The specific surface should have its energy lowered, rendering the crystal growth along its direction more probable.

Difference in the synthesis of $Fe_{50}Pt_{50}$ nanocubes (see A.1 page 68)

It is a common knowledge that in the synthesis of iron platinum, the molar quantity of iron precursor has to be twice more than the quantity of platinum precursor in order to obtain approximately $Fe_{50}Pt_{50}$ nanoparticles [25] since the iron atoms reduce the Pt contained in the $Pt(acac)_2$ precursor to Pt^0 and are oxidized to Fe^{+2} to form $Fe(acac)_2$.

In the case of $Fe_{50}Pt_{50}$ however, a diol had to be added to the synthesis. The diol acts as a reducer for $Pt(acac)_2$, preventing the iron from forming $Fe(acac)_2$ thus leaving more Fe^0 atoms to form nanoparticles.

Agregation of particles while annealing

The forces acting between nanocubes on a substrate form an equilibrium between attractive (Van der Waals) and repulsive (magnetic dipole-dipole interaction and steric repulsion). One clearly sees from the equations of the interaction energy of those 3 forces (see 4.1.3 page 13 determined for rounds nanoparticles) that when the temperature is raised:

- Van der Waals attractive interaction stays constant.
- Magnetic dipole-dipole repulsive interaction decreases when $k_B T$ becomes on the order of the magnetic anisotropy energy.
- Steric repulsion decreases linearly.

It is therefore clear that repulsive interactions are decreased at higher temperature whereas attractive interactions stay constant. Agregation of the nanocubes is a consequence of these interactions. Nanocubes situated inside a self-assembled area are organized with a local cubic ordering; which means that one of these nanocubes experiences a point symmetry centered on itself.

Repulsive and attractive interactions are then cancelled and no agregation with other nanocubes should theoretically occur. This explains why we observed that agregation starts from the edge of self-assembled areas.

Chemical ordering

Previous reports on the obtention of chemically ordered iron platinum alloys stated that the minimum annealing temperature required was 850 K [25]. In this work we report the partial chemical ordering of iron platinum in $L1_0$ phase at a temperature of 800 K (see A.4.2 page 74). This can actually be understood if we take a look at a diffusion process: we estimate the mean atomic diffusion length λ which is known to be a function of the annealing time τ_s and the diffusion coefficient D [38]:

$$\lambda = \sqrt{D\tau_s}\ [s] \tag{5.1}$$

The diffusion coefficient strongly depends on the diffusion constant D_0, the activation energy for diffusion E_a and the annealing temperature T_s :

$$D = D_0 e^{-\frac{E_a}{k_B T_s}}\ [cm^2 s^{-1}] \tag{5.2}$$

Since the diffusion of Fe atoms in a Pt matrix is faster than the other around, we consider this process more relevant to the kinetics of the ordering process, for which $D_0 = 2.1 cm^2 s^{-1}$ and $E_a = 3.0eV$. Moreover, $\lambda = 0.3$ nm for FePt alloy.

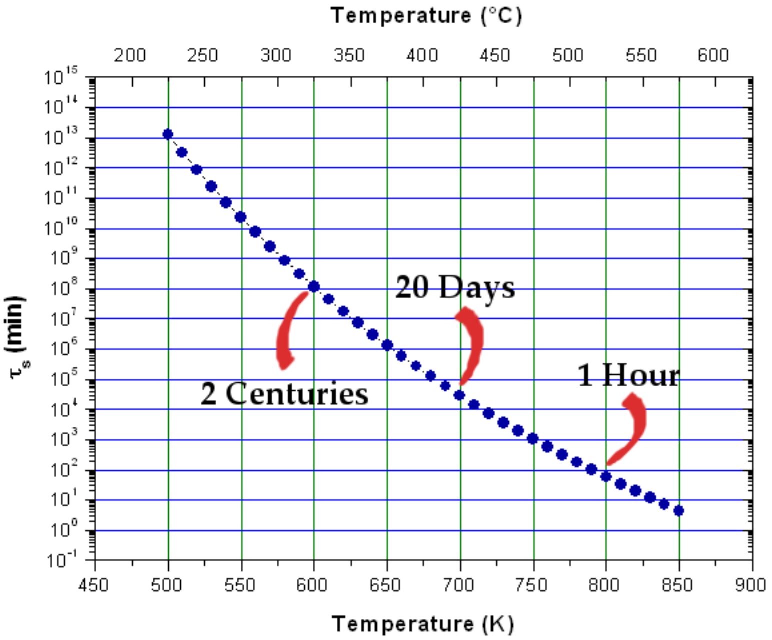

Figure 5.18: Time required to obtain $L1_0$ phase versus Annealing temperature

It is clear that depending on the temperature, the chemical ordering will take a different time to fully occur, however limited as can be seen in 4.1.4 page 15. In theory, the best procedure to chemically order a material is to anneal first up to the critical temperature and then very slowly (depending on the activation energy and the diffusion length it can take days or weeks) reduce the temperature. In our case, agregation needs to be avoided, so annealing at low temperature for a long time could be one solution to the present problem.

Chapter 6

Iron nanocubes

6.1 Synthesis and morphology of Iron nanocubes

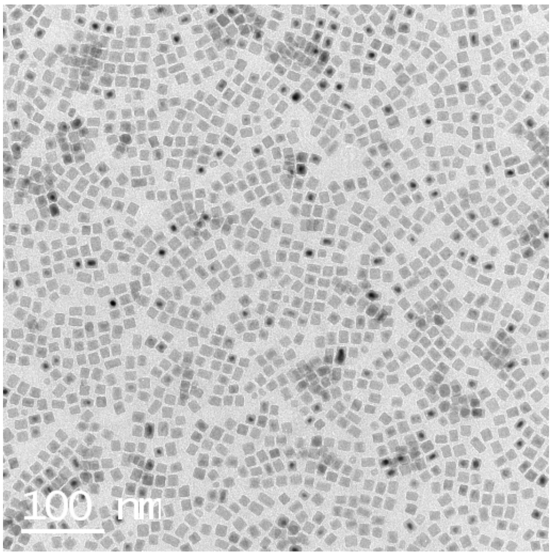

Figure 6.1: TEM overview of iron nanocubes

A publication from Franck Dumestre [39] shows a successful wet synthesis of Iron nanocubes with 7 nm mean edge lengths. The article does however not study the magnetic anisotropies nor the magnetic interactions of those particles so it will be the object of our present work.

The synthesis procedure for the iron nanocubes is as follows: $Fe[N(SiMe_3)_2]_2$ (1 mmol) is dissolved in mesitylene (20 mL) and heated up to 150°C for 48 hours in the presence of hexadecylamine (2 mmol) and oleic acid (1 mmol) under a dihydrogen atmosphere. A magnetic separation is performed in the solution and particles attracted by the magnet are the nanocubes. Then they are redispersed in heptane for further analysis.

This exact synthesis procedure was reproduced in our laboratory and led to nanocubes with however a mean edge length of 10 nm. A first sample was prepared by dropping a single drop of the colloidal solution on a standard copper grid covered with an amorphous carbon layer. As can be seen on Fig. 6.1, the cubes organize themselves with local cubic ordering but no global ordering is observed.

6.2 Texture

An electron diffraction experiment was performed on the previous sample to determine the presence of a texture in the array of nanocubes. Fig. 6.2 shows a diffraction pictogram with the substrate perpendicular to the electron beam i.e. 0^o.

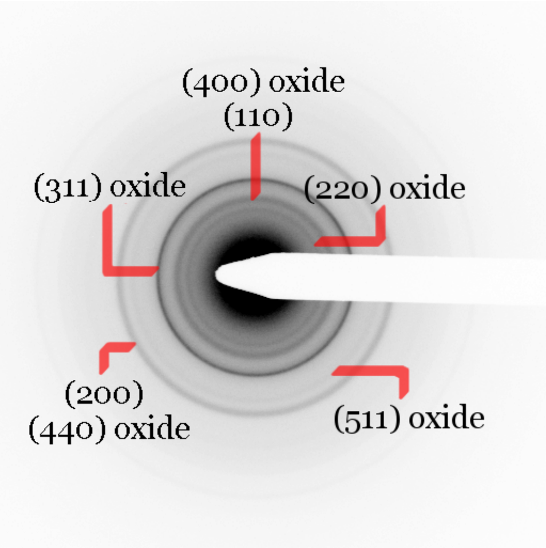

Figure 6.2: Electron Diffraction tilted @ 0^o of iron nanocubes

A simulation of an Xray powder diffraction has been performed using the Carine Crystallography software for a base centered cubic structure with the lattice parameter of bulk iron (2.8662 Å [40]) and is shown in Fig. 6.3.

As can be seen for a polycrystalline sample, the (200) peak is supposedly 5 times less intense than the (110) peak and approximately as intense as the (220) peak. However, since

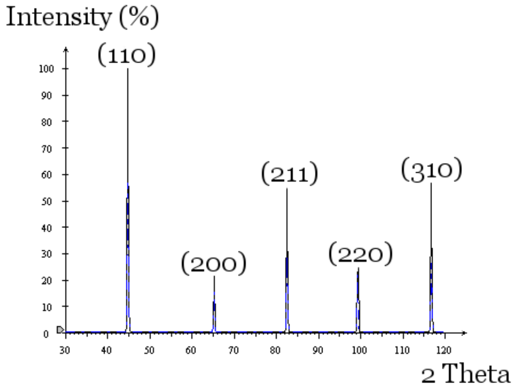

Figure 6.3: Powder diffraction simulation of bulk iron done with Carine Crystallography

one peak from iron oxide is overlapping with the (110) peak from iron, it is not possible to make a statement on a possible texture of the sample with respect to relative intensities of the diffraction peaks.

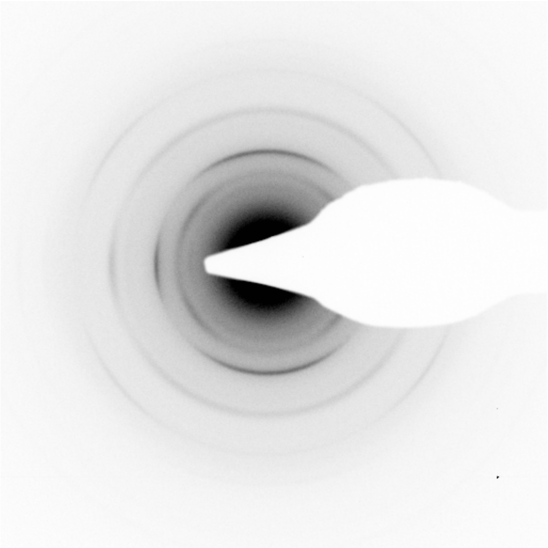

Figure 6.4: Electron Diffraction tilted @ 45^o of iron nanocubes

However tilting the sample makes the brightness of the different rings appear inhomogeneous (Fig. 6.4), as is typical when tilting the electron beam away from the texture direction when observing samples with a fiber-like texture. This texture is therefore in the axis of the viewing direction for which the rings are homogeneous, that is [001].

6.3 Structure

The structure of the iron nanocubes has furthermore been studied by High resolution electron microscopy and Xray diffraction. Fig. 6.5 shows a HRTEM picture showing atomic resolution of an iron nanocube with a Fourier transformation of the area within the red square as inset.

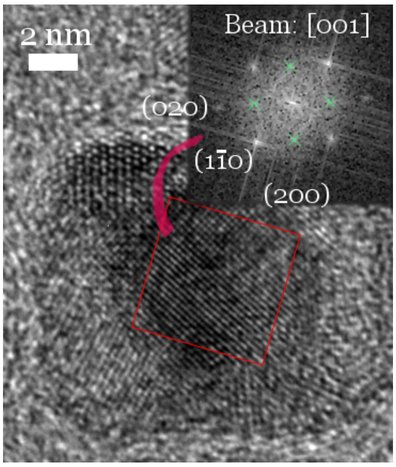

Figure 6.5: HRTEM pictogram of an iron nanocube with Fourier transformation of the iron core as inset

The nanocubes are core-shell particles with an iron core and an iron oxide shell which is rapidly grown when exposing the particles to air. The core has edges of ∼ 7 nm and appears darker on Fig. 6.5 while the oxide shell is between 2 and 3 nm thick and appears with a lighter contrast.

Iron core

It is clear from direct observation of Fig. 6.5 that the iron core is monocrystalline.

Analysis of the reflections in the core by local Fourier transformation of the high resolution pictures is tricky, because reflections from the oxide shell (from the top and bottom of the nanocubes) also appear due to the nature of the high resolution contrast[1].

---

[1] Without considering oxide reflections one can find a bcc structure with a ∼ 4.10 Å for iron.

However, taking into consideration this fact, the structure we find for the iron core is base centered cubic with a mean lattice parameter of $a = 3.03$ Å $\pm$ 0.05 Å which corresponds to an expansion of $\sim 5\%$ from bulk value.

The direction of growth for the iron core are the (100) family planes which are the cube facets' planes.

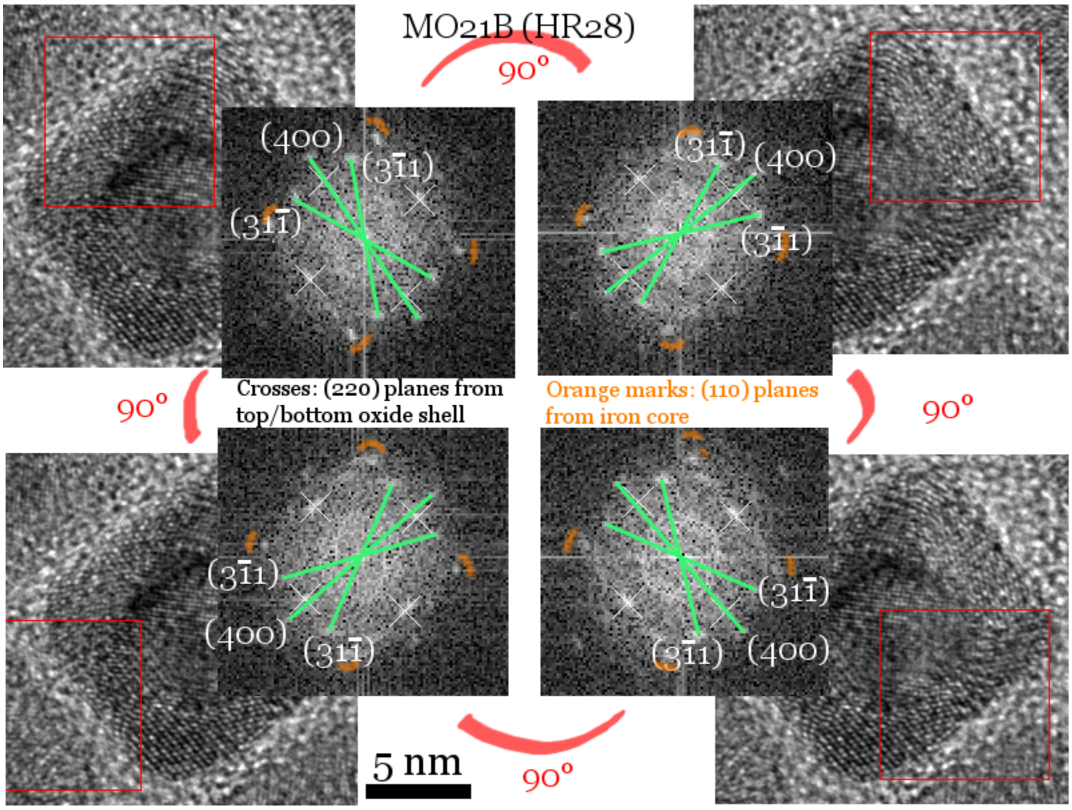

Figure 6.6: Structure analysis of iron oxide shell of nanocubes

Iron oxide shell

Analysis of multiple high resolution images has not allowed to determine the precise structure of the oxide shell that is either magnetite (Fe_3O_4) or maghemite ($\gamma - Fe_2O_3$)[2] which have both an inverse spinel structure. However Dumestre claims that this shell is magnetite in [39].

---

[2] Diffraction peaks from both oxide structures are very closer one to each. One way to determine this would be to anneal the samples under inert atmosphere, because maghemite turns to haematite ($\alpha - Fe_2O_3$at ~ 713 K.

Fig. 6.6 shows a structure analysis of the iron oxide shell. Reflections shown (311) and (400) family planes come from the lateral oxide shell, while the white crosses are reflections coming from the top and bottom oxide shells. This last statement can be made according to the fact that when making a local Fourier transformation of the iron core, those reflections are still visible.

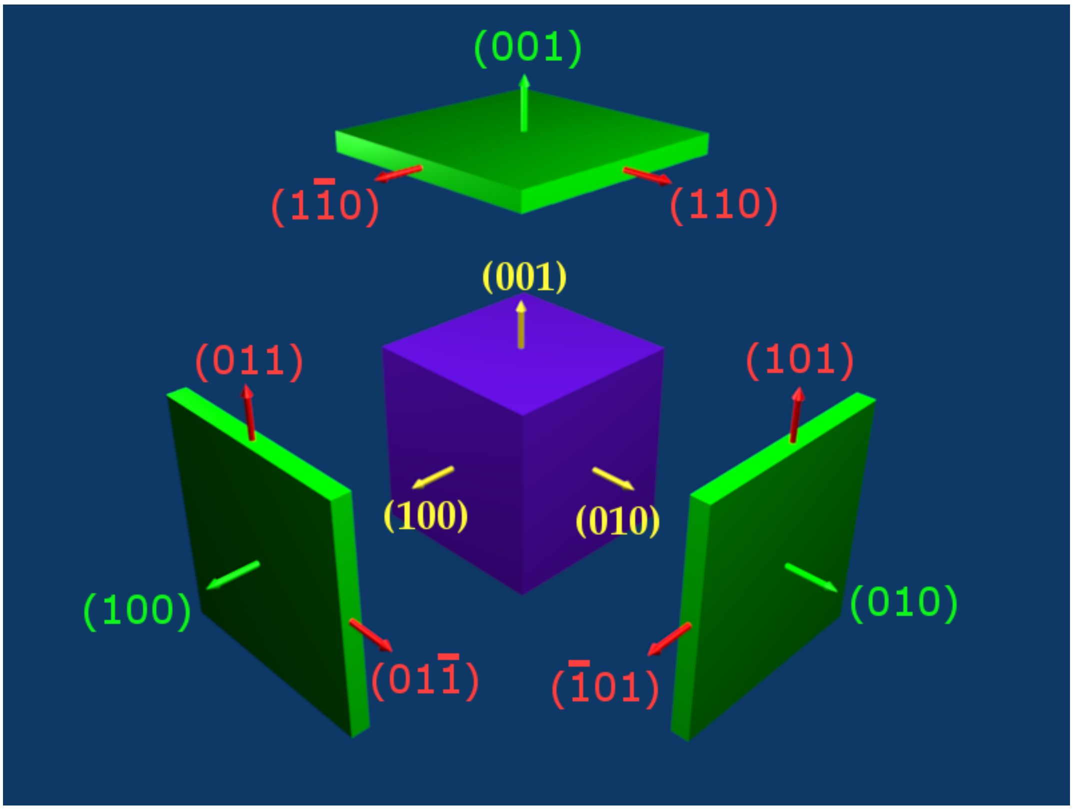

Figure 6.7: Sketch of an Iron nanocube structure

From the angles between the reflections for each lateral oxide shell it is clear that the oxide shell is polycristalline and that each facet of the cube is a monocrystal connected with neighbouring crystals by grain boundaries. The normals of the oxide shell's facets are all (100) family planes, which means that the direction of the oxide growth is consistent with the iron core growth. A sketch of an iron nanocube's structure is shown in Fig. 6.7 with the iron core in blue and the iron in green. Each separate element is single crystalline and the arrows show crystallographic directions.

Lattice parameter determined by high resolution micrograph is $a = 8.74$ Å ± 0.15 Å which is consistent within 4% of bulk value for Magnetite (a = 8.39 Å) and 5% of bulk Maghemite (a = 8.34 Å).

Electron diffraction calibrated with a thin film gold sample has also been performed in the Philips CM-12 to confirm the structures and lattice parameters of both iron core and iron oxide shell:

- *For iron cores:* according to the 2 visible rings (110) and (200) a = 2.91 Å ± 0.06 Å which corresponds to an increase of ~1.5% from bulk value.
- *For iron oxide shells:* according to the visibles rings (220), (400), (311), (511) and (440) a = 8.39 Å ± 0.16 Å which is exactly centered on the bulk value for Magnetite. The error bar does not allow us to conclude between Magnetite and Maghemite.

6.4 Magnetic properties

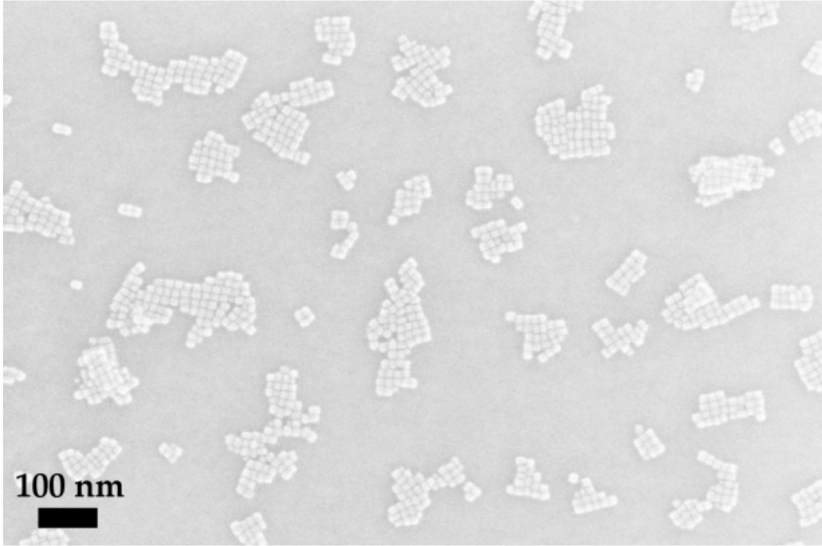

Figure 6.8: SEM overview of iron nanocubes on a silicon wafer

Ferromagnetic resonance angular dependence experiments have been conducted in order to determine the magnetic anisotropies of the iron nanocubes. It is usually not possible to determine magnetocrystalline anisotropy of nanoparticles using this method because their crystallographic axis are not aligned. However, since the iron nanocubes deposit on surfaces with a strong [100] texture, it should be possible to determine it.

A sample has been prepared by spin coating at 3000 rpm during 30 seconds a single drop of concentrated solution of iron nanocubes on a 4 mm × 4 mm boron doped silicon substrate. A representative SEM picture of the sample is shown in Fig. 6.8: the nanocubes are organized in small 2 dimensional clusters or "islands" that are separated by a distance between 100 nm and 200 nm.

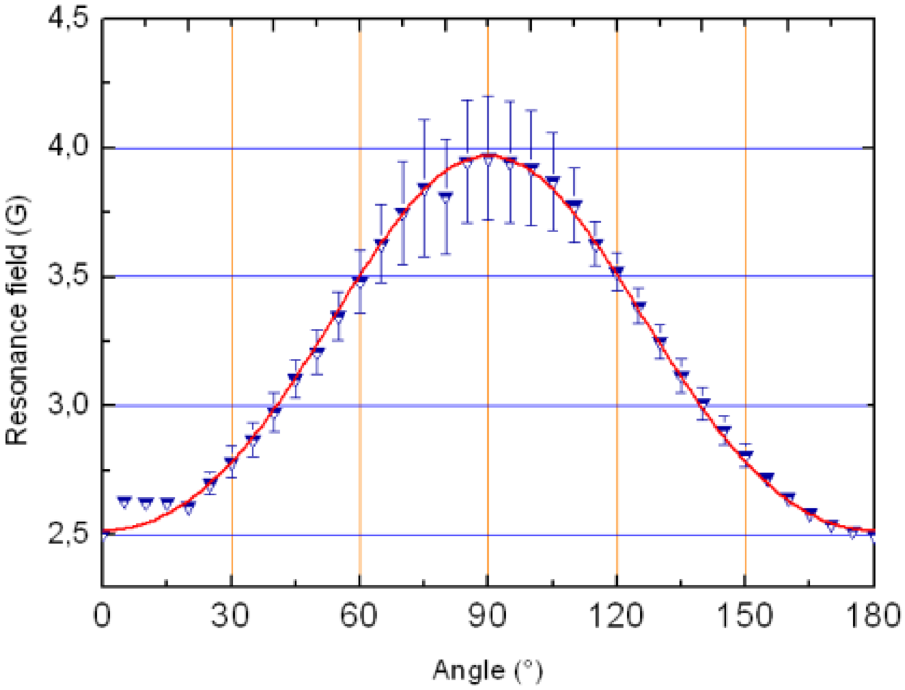

Figure 6.9: Out of plane angular dependence of resonance field

The FMR experiments have been conducted in a Bruker EPR spectrometer with an X-band cylindrical cavity. The sample holder had an included manual goniometer with a precision of ± 0.5^o. The experiment was started with the external constant magnetic field in the silicon substrate plane, although the absolute value of the angle with respect to this plane can not be found precisely with the goniometer. Subsequent adjustments have been made during data analysis[3]. Gas nitrogen was continuously flowing on the sample to prevent the electron resonance of oxygen.

All the obtained FMR spectra were then each fitted with a one line Gaussian derivative distribution[4] then the resonance field and corresponding linewidth was extracted for each

---

[3] The substrate is a symmetry plane so the same symmetry has to be observed in the measurements.

[4] It is "common" to use Gaussian distribution for interacting particles and Lorentz distribution for non

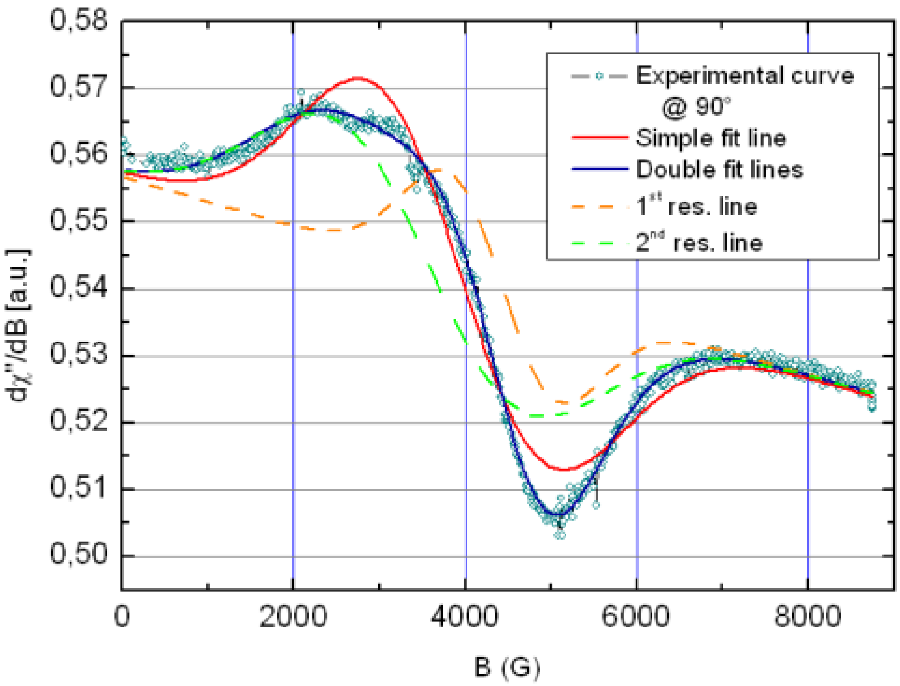

Figure 6.10: Resonance spectrum at 90^o from the substrate. The dashed lines are the ones used for the fit with 2 lines (in blue).

angle spectrum and the angular dependence graph was obtained on Fig. 6.9 on which 90^o corresponds to the out of plane direction, that is [001]. The consequent error on the resonance fields is due to the fact that there are actually more than one resonance field, but they are closer one to each other than rayleigh criterion, so it is not possible to fit them with more than one line. This problem is illustrated by Fig. 6.10.

The fit line for this graph was obtained using equation 4.22 with:

- $g = 2.00$ (for bulk iron it is 2.09 [41]). It would however be necessary to do multifrequency measurements to determine the exact value of g.
- $\frac{K_{2\perp}}{M} - \frac{1}{2}\mu_0 f M = 0.49$ Tesla where f is the filling factor of the sample
- $\frac{K_{4\perp}}{M} = 0.014$ Tesla

Using the magnetization of bulk iron ($M = 1.71 \times 10^6\ A/m$ [41]) and considering that the "islands" of nanocubes are not interacting with each other, it is possible to calculate the anisotropy constants:

---

interacting particles.

- $K_{2\perp} = 1.49 \times 10^6\ J.m^{-3}$ with $f = 0.36$ (determined by analysis of SEM pictures)
- $K_{4\perp} = 2.39 \times 10^3\ J.m^{-3}$

6.5 Further discussions

Organization of the cubes

If one compares the pictures of the self-assembled nanocubes of the original article [39] and Fig. 6.1 it seems that the organization is clearly worse in the case of our synthesis. The process for sample preparation is however different:

- Dumestre et al. have directly used the synthesis nanocubes without redispersing them: some particles formed supercrystals in the solution and those were directly deposited on a TEM grid by dropping the solution.
- We first redispersed the particles in heptane, separating the supercrystals and then deposited them on a TEM grid.

Our method clearly destroys the supercrystals formed in solution and shows the real properties of self-assembly of a substrate, which explains why this assembly is more local in our case.

Error on magnetic anisotropies

It is surprising that such a high uniaxial magnetic anisotropy was determined. Therefore it is interesting to have an order on the error committed on the magnetic anisotropies. In fact the relative error should be quite big due to:

- The experimental error due to FMR measurement and fitting of the FMR spectra.
- The number of parameters used to fit the angular dependence of resonance field spectrum (at least g should be determined by multifrequency measurements).
- The filling factor has been determined by SEM pictures and by considering that the clusters of nanocubes do not interact with each other.
- Bulk magnetization for iron has been used for calculation.

Considering a perfect fit (which is far from reality) we can calculate with $\frac{\Delta f}{f} = 5\%$ and $\frac{\Delta M}{M} = 50\%$:

$$\Delta K_{2\perp} = (F + \mu_0 f M)\,\Delta M + \frac{1}{2}\mu_0 M^2 \Delta f \tag{6.1}$$

Where F = 0.49 Tesla (value used for fitting). This gives $\frac{\Delta K_{2\perp}}{K_{2\perp}} \approx 78\%$. The uncertainty on this value is therefore very big and mostly due to the uncertainty on the magnetization. Determining the magnetization of the sample is therefore a priority for the analysis of the magnetic anisotropies.

Magnetic properties

Magnetic anisotropies determined by FMR measurements show interesting values:

Macroscopic structure	$K_{2\perp}$ (10^5 $J.m^{-3}$)	$K_{4\perp}$ (10^5 $J.m^{-3}$)
Bulk	-	0.47
Iron nanocubes	14.9	0.0239
Iron thin film grown on GaAs(100) 5 monolayers	11.53	0

Table 6.1: Magnetic anisotropies of iron for different macroscopic structures (bulk values from [41])

Bulk iron does not have any uniaxial anisotropy constant ($K_{2\perp} = K_{2\parallel} = 0$) due to its cubic 4-fold symmetry. However it is known that for iron thin films the surface and interface anisotropies can induce a $K_{2\perp} \neq 0$ due to a loss of symmetry at the interface and a modification of the electronic orbitals.

However the iron nanocubes have an iron core of 7 nm, or a thickness of approximately 48 monolayers, that means that the surface to volume ratio of atoms is 12 % considering that no reconstruction occurs at the iron oxide/iron interface. This value does not allow us to interpret this increase in uniaxial anisotropy as only a surface effect, since even for an iron 5 monolayers thin film grown on GaAs(100) $K_{2\perp}$ is found to be smaller. As I already discussed, the real uniaxial anisotropy constant is most probably smaller than what has been approximately determined, but the idea is the same.

One hypothesis is that a ferromagnetic or antiferromagnetic exchange coupling appears at the iron/iron oxide interface, causing an additional exchange field ($K_{eff} = 10^4 -$

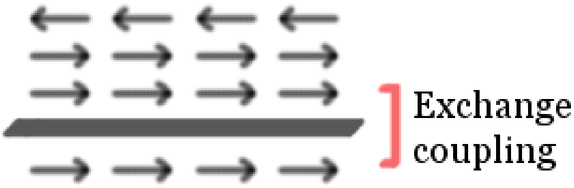

Figure 6.11: Ferromagnetic exchange coupling between a ferrimagnet (top) and a ferromagnet (bottom)

10^5 $J.m^{-3}$ for Magnetite, $K_{eff} = 10^5$ $J.m^{-3}$ for Maghemite) to be present in the direction of the coupling magnetization. This could be confirmed by annealing above the neel temperature of the iron oxide (850 K for Magnetite, 820 - 986 K for Maghemite) and cooling in an applied magnetic field so that the array of cubes would have a common magnetization direction for the iron oxide. A shift of the hysteresis should then be observed when measuring the magnetization of the sample versus magnetic field [42].

Chapter 7

Towards single particle ferromagnetic resonance

7.1 Foreword

The need to understand the physical properties of of nanoparticles has driven the development of new tools to probe the characteristics of individual objects on the nanoscale. Ferromagnetic Resonance (FMR) is a very powerful technique that allows one to measure magnetic quantities such as the Lande g factor, the FMR linewidth, the anisotropy field and even the magnetization. Traditional FMR setups are however optimized for large samples and are limited in their sensitivity down to 10^{11} paramagnetic moments. Considering the iron core of the Iron nanocubes seen in the previous chapter, it would correspond to $\sim 3.6 \times 10^6$ cubes.

Thus if we want to be able to probe single nanoparticles, FMR techniques showing increased sensitivity and eventually locally resolved capabilities need to be developed. This implies the use of either near-field techniques such as Magnetic resonance microscopy [44], Scanning tunneling microscopy [45] or optically detected magnetic resonance [46] or to develop new resonance cavities more suitable to samples whith lengths on the order of less than 100 nm [43]. This latter solution is to be investigated in the present work.

In its linear range, the sensitivity of an inductive detector is proportional to the quality factor Q and the filling factor of the cavity η. Because FMR requires a short recovery time if used for pulsed experiments, Q factor is not a desirable tuning factor and should stay at moderate values ($1000 > Q > 100$). The filling factor of a resonator can be increased by means of inserting high K dielectrics to better confine the magnetic field [47], or simply by reducing the size of the resonator structure. One design solution is the use of loop-gap resonators [48] with dimensions less than the resonant wavelength, which will be described in the following part of this report.

Planar microresonators, as reported by Narkowicz et al. [43] are quasi 2 dimensional loop-gap design coils at scales as small as 200 μm which can be fabricated by conventional optical lithography techniques.

In the context of locally resolved FMR setups, one major idea is to replace the ordinary resonant cavity of a locally detected FMR setup by a planar microresonator to enhance its sensitivity.

7.2 Microresonators design and analysis

The microresonator is based on the well known loop-gap design Fig. 7.1, which has been adapted to optical microlithography techniques: a planar copper coil is engineered on a dielectric substrate with two gaps on each side of the coil. The thickness of the copper coil is 35 μm.

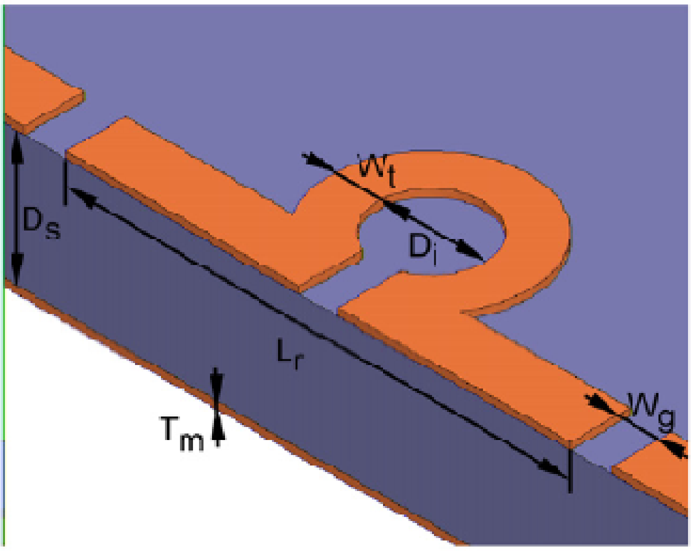

Figure 7.1: Schematic of a microresonator, from [43]

The gaps on both sides of the line (length W_g) allow one to adjust the absorption and quality factor of the resonator. The inner diameter of the coil (D_i) enhances the microwave efficiency factor when its size is reduced, as long as the width of the copper line (W_t) is kept small compared to it.

The idea behind this design is that, the smaller the inner coil diameter, the higher the microwave efficiency factor and the better confined the magnetic field hence a higher filling factor of the resonator.

However when considering a 200 μm coil to probe 10 nm long nanoparticles, one must be aware of the inhomogeneity of the generated magnetic field inside the coil that varies as 1/r where r is the distance to the coil inner edge, as can be seen on Fig. 7.2 which is a finite element method simulation of a PMR when current is applied. This means that depending on their position in the coil, the particles will receive a different amount of microwave power, resulting in inhomogeneities in the absorption.

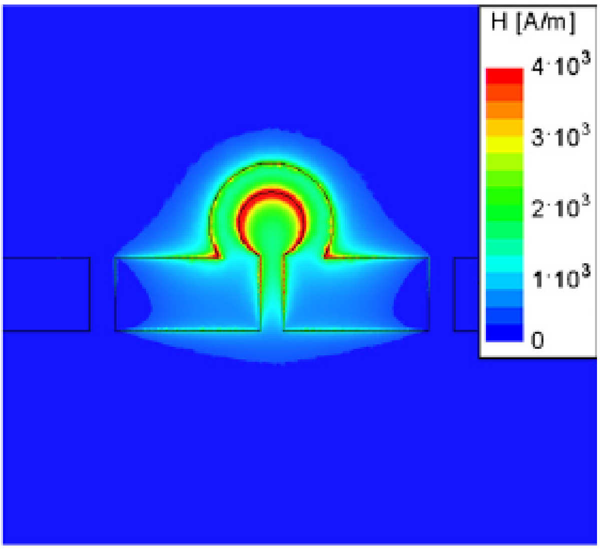

Figure 7.2: Finite Element simulation of a Magnetic field distribution of the microwave in the microstrip resonator with an integrated coil with a diameter of 500 μm, from [43]

In this specific design, the generated microwave is perpendicular to the substrate in the middle of the coil, and it has some small parallel component further away from the middle. Since the parallel component of the magnetic field is not totally zero, it might be possible to use it for out of plane angular dependent measurement, although the microwave power would be very small.

7.3 Experimental setup

Wet chemically synthesized Iron nanocubes [39] have been used as test samples to determine the sensitivity of the PMR and their possible applications with nanoparticles. The particles have an average length of 10 nm. They have been exposed to air and are therefore covered by a 2 to 3 nm oxide shell which could either be magnetite of maghemite, as revealed by High resolution TEM. They show the interesting property of assembling themselves on Silicon substrate and TEM Copper grids coated with amorphous carbon with a strong [100] texture, as revealed by Electron diffraction.

We used 2 different microresonators for our experiments, both manufactured on a ceramic (ref. R6010LM) which respectively have a 200 μm and a 500 μm inner coil diameter (D_i).

Due to time issues, a quick method of deposition not requiring any new setup was employed. Using an Eppendorf pipette to drop the colloidal solution was not appropriate for the application, since even with the smallest (5 μL) pipette, the size of the drop was way bigger than the 200 μm in diameter resonator, preventing us from being sure that most of the particles stay inside the coil.

The method chosen was to deposit the nanocubes on the microresonator using a hand-operated needle and a binocular. The needle was first dipped in the colloidal solution and was then quickly tapped in the middle of the coil with a sufficient precision, not allowing a drop to be formed on the tip. Depending on the elapsed time between dipping the needle in the colloidal solution and tapping it on the substrate and on the quantity of solution effectively kept on the needle, the number of particles deposited might vary. More reproducible methods such as AFM nanolithography or a simple mechanically controlled needle have to be considered in the event of further experiments.

Fig. 7.3 shows about a third of the area covered by the particles when using the needle method, in a single tap. Considering that the covered area is less than 50% and that in a fully covered 200 nm × 200 nm area approximately 50 cubes fit (determined with closer

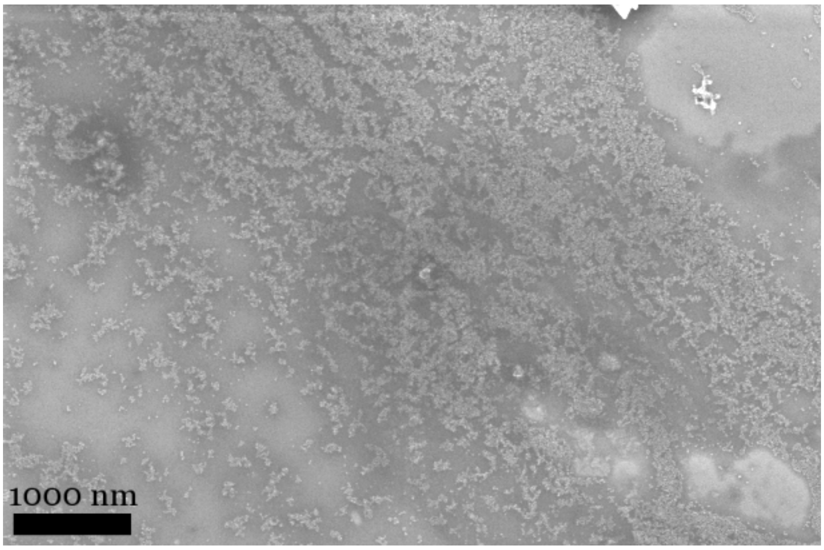

Figure 7.3: SEM picture of nanocubes deposited on a Silicon substrate using a needle

SEM view) we can roughly estimate the number of particles deposited to be on the order of *10000* per needle tap.

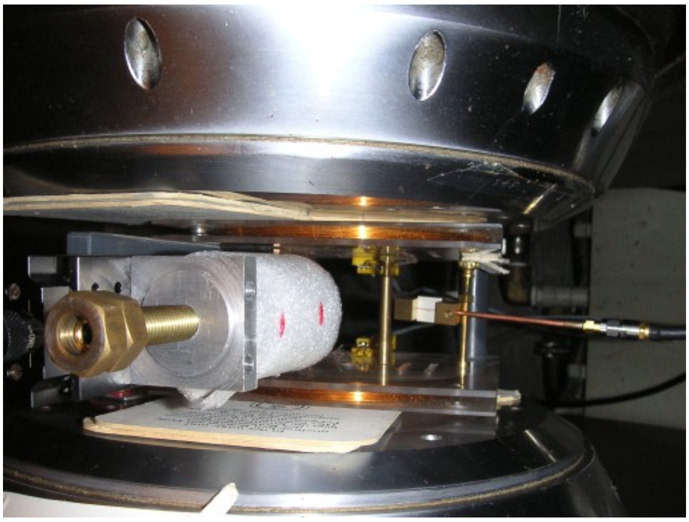

Figure 7.4: Photo of the FMR setup used in the university of Bochum

The whole FMR spectrometer was a simplified version of the setup used in the University of Dortmund that can be seen in [43]. A synthesizer used as the oscillator was connected to the planar microresonator through a circulator, which third end was directly connected to a lock-in amplifier. Reference frequency fed to the lock-in amplifier was achieved through field modulation by two coils that can be seen in Fig. 7.4.

The Planar microresonator was held by a small screw between two non magnetic metal pieces and the planar coil was connected to a waveguide through a small adjustable coupling antenna pressed on the microstrip line with silver paste to enhance the connection. (Fig. 7.5)

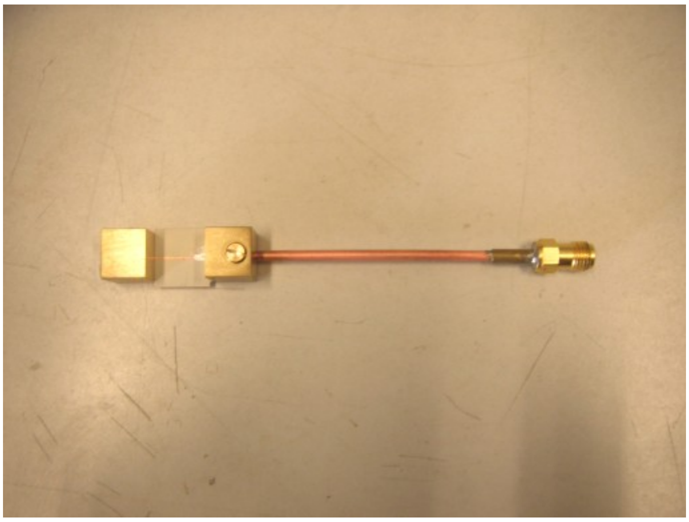

Figure 7.5: Photo of a microresonator inside its holder

The so-held PMR with particles in the middle of the coil have been taken to the Ruhr-University of Bochum, where it was placed as shown in Fig. 1 in the middle of two massive electromagnets that would generate the external magnetic field and two other small electromagnets that would generate the modulation field required for the frequency modulation of the lock-in amplifier. This setup has merely been designed to probe the capabilities of the PMR, since there is no way to precisely control the angle of the microresonator relatively to the external field. Angular dependent measurements were also out of the question, since no goniometer was installed.

7.4 Results: Sensitivity of the microresonator

The first question of real interest concerning these microresonators is the minimum detectable amount of spins. Answering this question precisely and quantitatively requires in a first step a method of deposition of the nanocubes in which we can control the amount of cubes in the middle of the PMR.

In order to be able to get a relative information on the concentration of particles inside the coil based on a sample in which the concentration is known, one needs to integrate two times the FMR signal if a modulation technique is used (because the derivative of the absorption) or just one time without any modulation. If all parameters are kept constant during all the experiments, then a simple ratio gives the relative number of spins within the coil. Knowing the characteristics of one average nanoparticle, it is therefore possible to get an approximate value of the number of particles probed.

However, as we saw earlier the microwave field is position dependent within the coil. This means that if the particles distribution is not homogenous withing the coil, and if the distribution is different for each measurement, an error is made. Determination of this error could be made by simulation.

As a first step, we have iteratively added particles inside the coil using a needle and done an FMR measurement to try and determine the minimum number of particles necessary to obtain a decent signal.

Two microresonators with an inner diameter of 500 μm resp. 200 μm were used for this experiment. Even after 16 taps of the needle each time dipped in the solution inside the 500 μm coil, no clear signal was obtained, merely a tendency within a noisy signal.

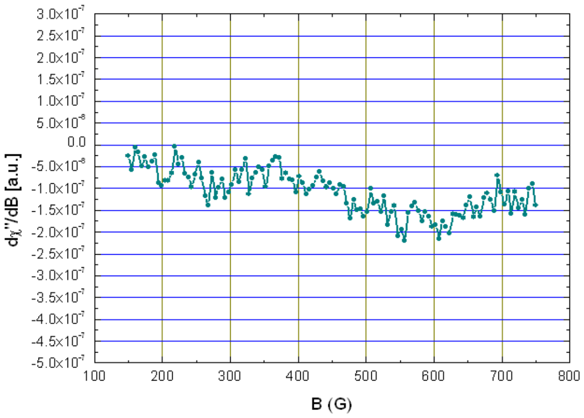

Figure 7.6: FMR signal with a 500 μm resonator after 4 taps of a needle

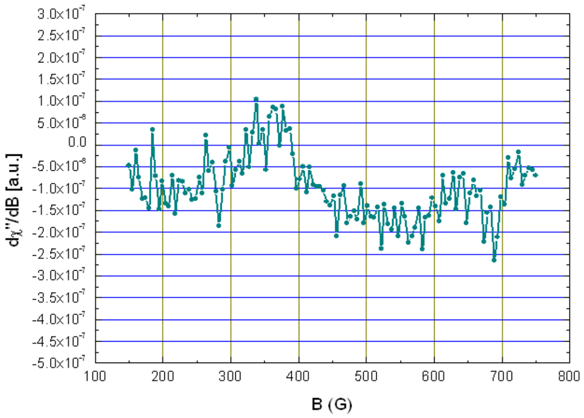

Figure 7.7: FMR signal with a 500 μm resonator after 16 taps of a needle

On the contrary, the 200 μm resonator proved itself really more sensitive, since using the same technique, a clear signal was obtained after only 4 taps of the needle (Fig. 6a compared to Fig. 7b).

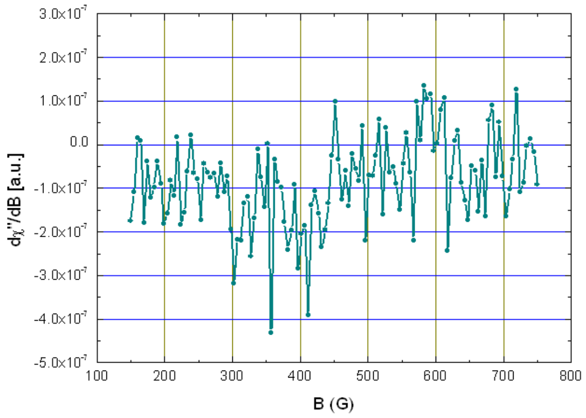

Figure 7.8: FMR signal with an empty 200 μm resonator

To sum up, the 500 μm resonator was not able to detect approximately 160000 iron nanocubes, whereas the 200 μm resonator was able to detect as few as 20000 iron nanocubes. This gives an increase of the sensitivity factor of ~ 8 for a decrease of the diameter of the resonator of 2.5. Reducing the diameter size of the resonator to increase its sensitivity is therefore an interesting way to investigate.

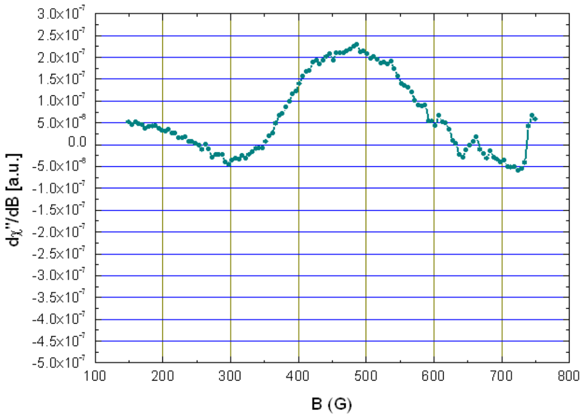

Figure 7.9: FMR signal with a 200 μm resonator after 4 taps of the needle

Compared to a normal cavity which can theoretically only detect down to $\sim\ 10^{11}$ paramagnetic spins, this is a major improvement since we could detect a paramagnetic resonance from only $\sim\ 6 \times 10^6$ paramagnetic spins, that is *more than 4 orders smaller.*

7.5 Future investigations

Should investigations continue on PMR, critical elements would need to be studied and developed so that those planar microresonators become a useful tool for FMR analysis of nanosized objects. Three separate topics should be the subject of studies.

As a first topic, a reproducible, effective method for the deposition of particles in the resonator should be studied, so that it would allow to:

- Deposit a well definite amount of particles on the substrate, with a minimum relative error.
- Be sensitive enough to bring the particles to a determined position within the coil, even for future designs with inner diameters smaller than 200 μm.

A second topic would be the evolution of the design of the microresonators. Many directions can be evaluated:

- Increase the sensitivity of the resonators by:
    - Reducing the coil size using for example electron lithography.
    - Possibly simulating new designs.
    - Changing the dielectric substrate for a better low-less dielectric with a smoother surface than the actual R6010LM.
- Increase the in plane component of the generated microwave to facilitate out of plane angular dependent measurements.

The third topic would consist of developing dedicated hardware for the microresonator:

- A special sample holder that would allow angular dependent measurements using a normal EPR setup.
- Adapt the microresonator to the locally resolved FMR setup to replace the standard cavity.

Chapter 8

Conclusion

In this work we report the wet synthesis of iron platinum nanocubes in the FePt and $FePt_3$ compositions and the synthesis of oxide-coated iron nanocubes. Crystallographic structures have been studied by High resolution TEM, Electron diffraction and X-Ray diffraction. Magnetic properties have been studied by SQUID magnetic susceptibility measurements and Ferromagnetic resonance.

Annealing experiments on as-synthesized nanocubes have shown interesting results concerning $L1_0/L1_2$ conversion and agregation properties. Magnetic properties of $FePt_3$ nanocubes are very interesting but require further experiments and analysis to give a detailed analysis. Several FMR measurements are also currently being conducted on iron nanocubes to determine more precisely the magnetic anisotropy constants.

We also report the successful use of planar microresonators for ferromagnetic resonance on nanoparticles which decreased the detection threshold of FMR down to $\sim 6\times10^6$ spins.

This work was very interesting from a scientific point of view. I have been able to apply most of my knowledge and methods acquired during my education. The highlight that I will remember from this work is that learning to learn is the most important thing in one's education.

From a human point of view I have had the opportunity to discover the small world of scientific research, in which I have really felt free to work in directions that I had chosen myself. Most of all, taking care of practical works was a really enriching experience. Explaining to others helps you check and improve your own understanding.

Appendix A

$\mathrm{Fe_{50}Pt_{50}}$ nanocubes

A.1 Synthesis and morphology

The obtention of FePt nanocubes with a mean composition of $Fe_{50}Pt_{50}$ was however impossible to obtain using this synthesis method by varying the concentrations of precursors nor ligands.

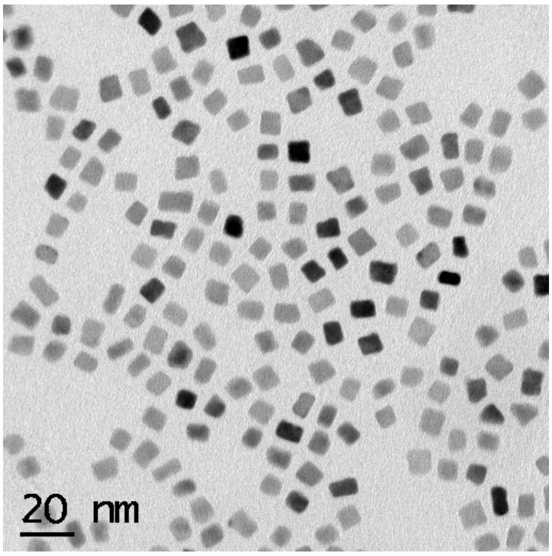

Figure A.1: Overview of as synthesized FePt nanocubes

After different tries, we found out a synthesis procedure which allowed the particles to be stabilized in a cubic shape with a composition in the $L1_0$ range: In inert atmosphere $\mathrm{Fe(CO)_5}$ (0.66 mmol), $\mathrm{Pt(acac)_2}$ (0.33 mmol), Oleic acid (4 mmol), Oleylamine (4 mmol)

Number	Fe (%)	Pt (%)	σ (%)
1	56.84	43.16	0.89
2	51.46	48.54	1.13
3	59.97	40.03	1.02
6	57.93	42.07	0.93
8	51.15	48.89	0.89
9	54.73	45.27	1.25

Table A.1: Analysis of the FePt nanocubes by microprobe EDX

are diluted in Dichlorobenzene (solvent, 15 mL) with the addition of 1,2-hexadecanediol (0.66 mmol). The mixture is directly heated up to a reflux temperature of 170°C during 24 hours. A standard washing procedure is then applied to remove the smallest particles and remove the excess of ligands.

The reduction of Pt(acac)$_2$ by a diol increases the nucleation process while preventing the growth process to incorporate too much platinum in the initial seeds. Therefore, cubic nanoparticles with a higher concentration of platinum in the composition can be obtained. They can be seen on Fig. A.2.

Energy Dispersive Xray (EDX) spectroscopy using the TEM microprobe mode first allowed us to probe the mean concentration of the nanocubes. Results given in table A.1 show a relative mean composition of the particles of 55.35% iron and 44.65% platinum with a standard deviation s = 3.56%.

EDX in nanoprobe mode allowed us to probe local areas with few nanocubes. The results given in table A.2 show a relative mean composition of the particles of 43.05% iron and 56.95% platinum.

The big difference (more than 10% in composition) between microprobe and nanoprobe results can be explained by many possibilities:

- When using nanoprobe, the electron beam is so intense that it has the tendency to decompose the excess of ligands that form a small layer on top of the particles. This forms a black spot on the image which absorbs the XRays coming from the nanocubes. Since the absorption of XRays is a function of their wavelength, it will

Number	Fe (%)	Pt (%)	σ
1	41.44	58.56	1.70
2	46.02	53.98	1.81
3	44.25	55.75	2.02
4	45.11	54.89	1.99
5	42.11	57.89	1.69
6	40.46	59.54	1.74
7	41.99	58.01	2.31

Table A.2: Analysis of the FePt nanocubes by nanoprobe EDX

be different for iron and platinum, leading to an error in the composition. However when analysing this sample, no significant black spot was formed.

- When using microprobe, the XRays come from all the illuminated part of the sample. This means that even badly shaped particles which probably have a different composition and non decomposed precursors also give an EDX signal, also leading to an error in the composition of the nanocubes.

We can therefore think that the ”true” results are closer to the *nanoprobe* results than the microprobe results.

A.2 Structural properties

A standard TEM copper grid coated with an amorphous copper thin film was prepared with FePt nanocubes. Fig. A.3 shows a high resolution electron micrograph of a single FePt nanocube taken with a Tecnai F20 Supertwin. Analysis by Fourier transformation allows us to index the spatial frequencies of the cube and compare them with known tables of usual structures. Since the nanocubes should be in the chemically disordered phase, the structure should be face centered cubic.

Analysis of the angles between the family planes of the nanocubes and their lengths for 14 different nanocubes of a same sample allows to confirm the chemically disordered fcc structure and determine the crystallographic orientations (see inset of Fig A.3). The absence of forbidden fcc reflections confirms that the as prepared nanocubes are in the fcc disordered structure.

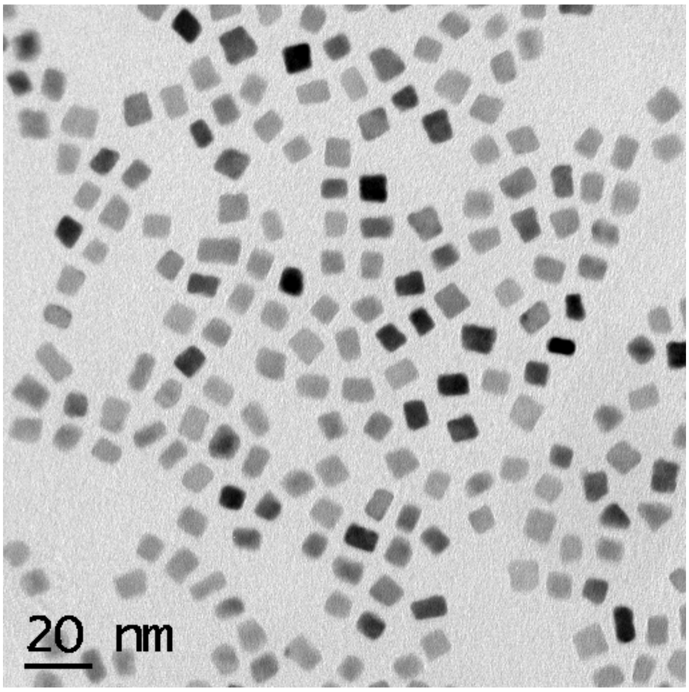

Figure A.2: TEM Overview of FePt nanocubes

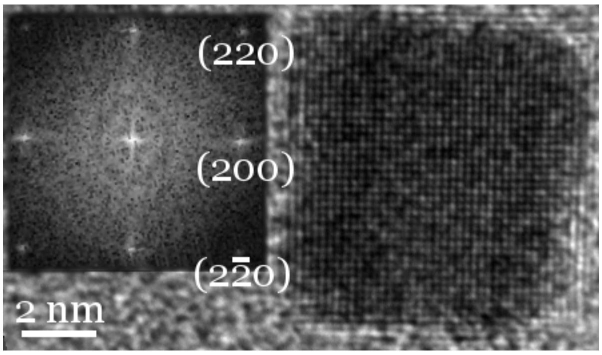

Figure A.3: High resolution pictogram of a FePt nanocube with Fourier transformation as inset (direction of the electron beam: [001])

All the nanocubes analyzed were single crystals with a mean lattice parameter of a = 3.97 Å with a standard deviation s = 0.07 Å. Litterature value for the lattice parameter of bulk $Fe_{50}Pt_{50}$ is a = 3.82 Å [23] which gives a lattice expansion of 3.9% for the nanocubes which is the same expansion value found for the $FePt_3$ nanocubes.

Electron Diffraction has then been performed on the same TEM grid in the Philips CM-12. Calibration of the camera constant was done by exchanging the FePt sample with

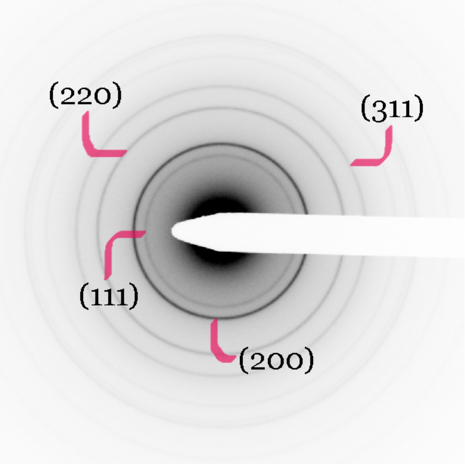

Figure A.4: Electron Diffraction picture of FePt nanocubes

a gold thin film on a copper grid which diffraction peaks are known. The value determined by measurement of the four first diffraction rings was a = 3.89 Å ± 0.08 Å [31] with a standard deviation s = 0.002 Å.

A.3 Texture

The electron diffractogram (Fig. A.4) shows a (200) diffraction ring with a clearly higher intensity as the (111). Since the structure of chemically disordered FePt is the same as $FePt_3$ except for a different lattice parameter,Fig. 5.8 also shows that the (111) intensity should be almost twice as big as the (200) intensity of a polycrystalline sample. This is a first evidence of a (100) texture.

Tilting the sample to 45^o also displays inhomogeneities in the diffractions rings, bringingthe same conclusions as those of $FePt_3$ nanocubes, confirming the strong (100) texture.

A.4 Annealing

A.4.1 $L1_0$ phase

In-situ annealing of a sample of FePt nanocubes prepared on a standard copper TEM grid coated with a copper thin film was done in the Philips CM-12 TEM in order to confirm our asumption that the particles effectively possess the FePt structure. If the $L1_0$ phase would appear when annealing above 580^o [25] then we would have a definite evidence of this fact.

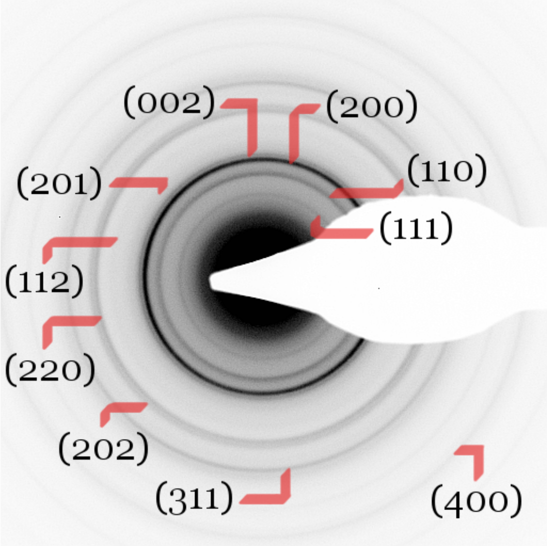

Figure A.5: Electron Diffraction picture of FePt nanocubes after annealing at 700^oC tilted @ 0^o

Starting from room temperature, the sample was heated up to 700^oC with steps of 20 minutes each 50^oC. No pre-annealing in inert atmosphere was done to decompose the ligands at the surface of the cubes, since the only purpose of this experiment was to determine the presence of cubes in the $L1_0$ composition range.

Fig. A.5 shows an electron diffraction picture taken after annealing. It is clear that the crystallographic structure is different from before annealing. Analysis of the ratios between all the rings allowed to determine the family of planes from which they stem by comparison with a simulation done with Carine Crystallography.

With a relative error between 0.7% and 3.3% all the rings correspond to $L1_0$ family planes and none corresponds to any $L1_2$ family planes, which confirms that most of the nanocubes are effectively in the FePt composition range.

A.4.2 Magnetic field annealing

Magnetic field annealing of iron platinum nanoparticles should theoretically:

- Enhance the chemical ordering of the alloy [36].
- Prevent aggregation of the nanoparticles by providing dipole-dipole repulsion forces.

Annealing of the same nanocubes has also been performed with and without magnetic field without varying other parameters in order to determine the effect of the magnetic field. Two identical samples were prepared on 2.3 mm diameter TEM copper grid with a carbon thin film coating. A stainless sample holder was specially crafted so that it could fit inside a SQUID with an oven installed. The TEM grid was placed horizontally in the sample holder, so that the magnetic field was perpendicular to the grid. The SQUID would only be used for its magnet and not its measuring capabilities. Gas helium was continuously flowing during the experiment.

For the first sample, the magnetic field was set to 5 Tesla at room temperature and the temperature was then raised up to 800 K at 5 K/min and waiting 30 min each 50 K (maximum safe temperature for the SQUID). The temperature of 800 K was kept for 6 hours and then the same ramping of temperature was done down to room temperature.

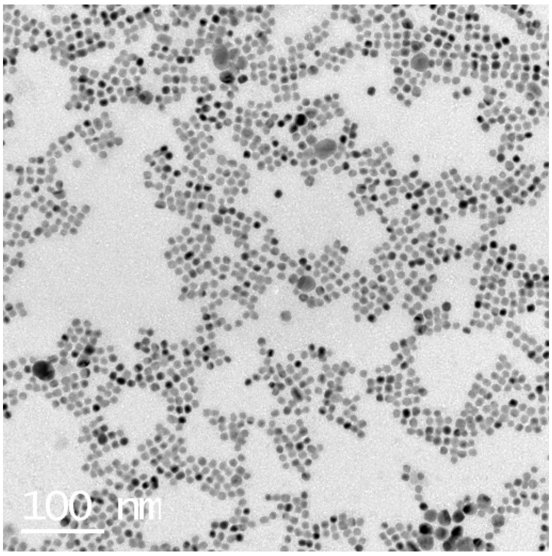

Figure A.6: FePt nanocubes after annealing with a 5T magnetic field

This exact procedure was repeated on the second sample without magnetic field. A TEM picture of the nanocubes annealed with magnetic field is shown in Fig. A.6 and without magnetic field in Fig. A.7.

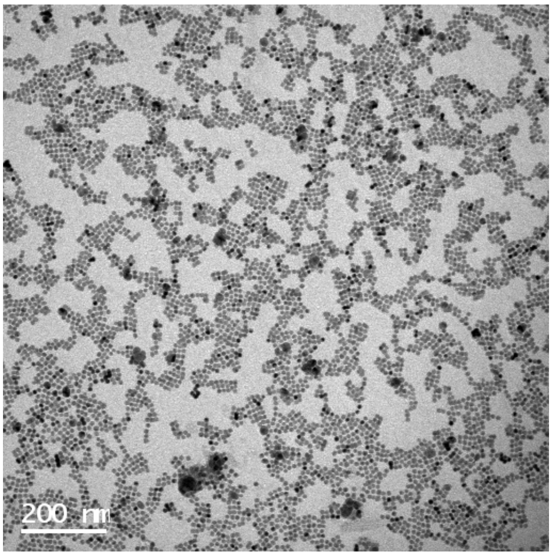

Figure A.7: FePt nanocubes after annealing without magnetic field

By comparing the two pictures, it is not clear whether the magnetic field has had an effect or not and we cannot make any statement regarding our previous hypothesis. However, (figure not shown) the $L1_0$ phase is already present after both annealing experiments with less agregation than what can be seen in Fig. 5.14 after annealing at 850 K.

A.5 Further discussions

Magnetic Field annealing

Improvement of $L1_0$ ordering

The mechanism for the improvement of chemical ordering by magnetic field annealing is not totally understood. One possible explanation is that the Curie temperature $T_{C.L1_0} =$ 750 K the $L1_0$ phase and for $A1_0$ phase $T_{C.A1_0} = 600$ K.

Therefore for $T_{C.L1_0} >$ T $> T_{C.A1_0}$ if a magnetic field is applied, the free energy o the $L1_0$ phase is reduced by $F = -M.H$ where M is the magnetization of the alloy and H is the applied magnetic field. This magnetic energy is thought to be the driving energy for the phase transformation [36].

However since the $L1_0$ transformation was reported to be a nucleation and growth process [37], the single crystalline nanoparticles must inhibit this nucleation in some way.

Agregation prevention

The failure of this experiment can be explained by a simple dipole-dipole energy calculation between two magnetic moments. Considering a magnetic field applied along z (z being the normal to the substrate) and considering an average of 7 nm cubes separated center-to-center by $r = 10$ nm we can calculate:

$$H_{DD} = \frac{\mu_0}{4\pi r^3}\mu_{Max}^2$$

Where $\mu_{Max} \approx 3.43 \times 10^{-19} A.m^2$ (using an average atomic moment $\mu_{At} = 1.43\mu_B$ [23]) is the magnetic moment of a single average nanocube, we obtain then:

$$H_{DD} \approx \frac{4\pi \times 10^{-7}}{4\pi(10^{-8})^3}(3.43 \times 10^{-19})^2 \approx 11.77 \times 10^{-21} J = 850K$$

This calculation is far from reality since it considers the dipolar interaction between two perfect points and with a saturated magnetization. However it gives an order of the maximum interaction energy between 2 cubes which is on the order of the annealing temperature. This gives a first approximation on why the dipole-dipole repulsion did not prevent agregation of the nanoparticles.

Appendix B

Teaching

During my work I had the opportunity to be *Betreuer* (tutor) in charge of the following practical works:

- Bestimmung der spezifischen Ladung $\frac{e}{m}$ (Determination of the specific charge of the electron $\frac{e}{m}$)
- Heissluftmotor (Hot air machines)
- Messung mit der magnetischen Drehwaage (Measure with a magnetic couple)
- Geschwindigkeit von α-Teilchen (Speed of α particles)
- Temperaturstrahlung (Radiation from heated bodies)
- Elektrischer Widerstand von Metallen und Halbleitern (Electric resistance of metals and semiconductors)
- Laser-Interferometer

Which included 71 hours of laboratory work and countless hours spent correcting the students' protocols which were handwritten in German.

Appendix C

Nano heart

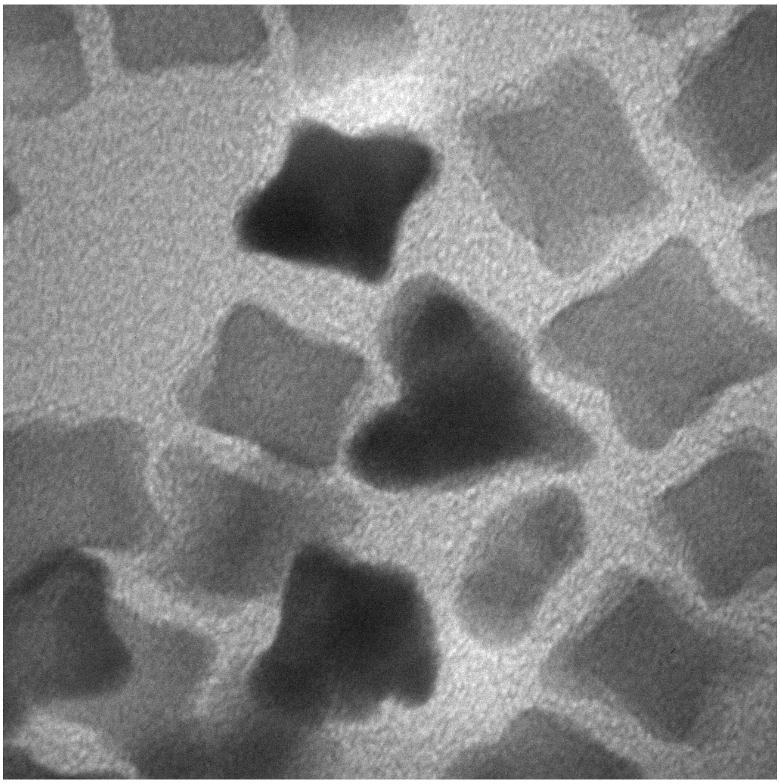

A new startup company ”Nanolove” has been founded and Nano Hearts should be ready for delivery by February, 14. 2007.

”A Nano Heart is like real love: you can’t see it but your wallet can.”

Bibliography

[1] Cordente, N. (2001) ”Synthesis and Magnetic Properties of Nickel Nanorods” *Nano Letters* **1**: 565.

[2] Snoeck, E. (2002). ”Quantitative magnetization measurements on nanometer ferromagnetic cobalt wires using electron holography” *Applied Physics Letters* **82**(1): 88.

[3] Victor F. Puntes (2000). ”Colloidal Nanocrystal Shape and Size Control: The Case of Cobalt” *Science* **291**(5511): 2115 - 2117.

[4] Rellinghaus, B. (2002). ”Self-Assembled Structures of Gas-Phase Prepared FePt Nanoparticles.” *Mat. Res. Soc. Symp. Proc.* **705.**

[5] Amoruso, S., G. Ausanio, et al. (2005). ”Femtosecond laser pulse irradiation of solid targets as a general route to nanoparticle formation in a vacuum.” *Physical Review B* **71**(3): 033406.

[6] Lamer (1952). ”Nucleation in Phase Transitions.” *Industrial and Engineering Chemistry* **44**: 1270.

[7] Park, J. (2001). ”Model of Formation of Monodispersed Colloids.” *Journal of Physical Chemistry B* **105**: 11630.

[8] Herring, C. (1951). ”Some theorems on the free energies of crystal surfaces.” *Physical Review* **82**(1): 87 - 93.

[9] Stappert, S. (2003). ”FePt-Nanopartikel aus der Gasphase: Herstellung, Struktur und Magnetismus.” *PhD thesis from the University of Duisburg-Essen.*

[10] Kittel, C. (1948). ”On the Theory of Ferromagnetic Resonance Absorption.” *Physical Review* **73**(2): 155.

[11] Scherer, C. (2005). "Ferrofluids: Properties and Applications." *Brazilian Journal of Physics* **35**(3A): 718 - 727.

[12] Rosensweig, R. E. (1985) "Ferrohydrodynamics" *Cambridge Univ. Press*

[13] Saita, S. (2005). "FePt Nanoparticles with a Narrow Composition Distribution Synthesized via Pyrolysis of Iron(III) Ethoxide and Pt(acac)2." *Chemical Materials* **17**: 3705 - 3710.

[14] T.J., K. (2003). "Combined reactions associated with L10 ordering" *Journal of Magnetism and Magnetic Materials* **266**: 79 - 87.

[15] Van Vleck, J. H. (1937). "On the Anisotropy of Cubic Ferromagnetic Crystals." *Physical Review* **52**(11): 1178.

[16] Antoniak C. (2005). "Magnetic anisotropy and its temperature dependence in iron-rich FePt nanoparticles." *Europhysics Letters* **70**(2): 250 - 256.

[17] Respaud, M., J. M. Broto, et al. (1998). "Surface effects on the magnetic properties of ultrafine cobalt particles." *Physical Review B* **57**(5): 2925.

[18] Williams, D. B. (1996). "Transmission Electron Microscopy: a textbook for materials science" *Plenum Press.*

[19] Farle, M. "Ferromagnetic resonance of ultrathin metallic layers" *Rep. Prog. Phys* **61**(755): 1998.

[20] Salaba,E. "Structural and Magnetic Investigations of Magnetic Nanoparticles and Core-Shell Colloids" *PhD thesis in the University of Duisburg-Essen* 2004.

[21] Oliver, S. A. (1988). "Magnetic resonance experiments on ion beam sputtered 100 Fe films." *Journal of Applied Physics* **63**(8): 3802.

[22] Clarke, J. (2004). "The SQUID Handbook Vol. I Fundamentals and Technology of SQUIDs and SQUID Systems" *Wiley-VCH.*

[23] Hayn, R. and V. Drchal (1998). "Invar behavior of disordered fcc-Fe$_xPt_{1-x}$ alloys." *Physical Review B* **58**(8): 4341.

[24] Stahl, B., J. Ellrich, et al. (2003). "Electronic properties of 4-nm FePt particles." *Physical Review B* **67**(1): 014422.

[25] Sun, S. (2000). "Monodisperse FePt Nanoparticles and Ferromagnetic FePt Nanocrystal Superlattices." *Science* **287**: 1989 - 1992.

[26] Chen, M. (2004). "One-Step Synthesis of FePt Nanoparticles with Tunable Size." *Journal of the American Chemical Society* **126**: 8394 - 8395.

[27] Shevchenko, E. (2002). "Colloidal crystals of monodisperse FePt nanoparticles grown by a three layer technique of controlled oversaturation." *Advanced Materials* **14**(4): 287 - 290.

[28] Howard, L. E. M. (2005). "A synthetic route to size controlled fcc and fct FePt nanoparticles." *Journal of the American Chemical Society* **127**: 10140 - 10141.

[29] Shukla, N. (2006). "Oriented self-assembly of cubic FePt nanoparticles." *Materials Letters* **60**: 995 - 998.

[30] Malm, J.-O. (1997). "Deceptive "lattice spacings" in high-resolution micrographs of metal nanoparticles." *Ultramicroscopy* **68**(1): 13 - 23.

[31] Schamp, C. T. and W. A. Jesser (2005). "On the measurement of lattice parameters in a collection of nanoparticles by transmission electron diffraction." *Ultramicroscopy* **103**: 165-172.

[32] Farle, M. "Some aspects in thin film magnetism."

[33] O'Grady, K. (1983). "Curie-Weiss behavior in ferrofluids." *Journal of Magnetism and Magnetic Materials* **31-34**(2): 958.

[34] Litvinov, D. (1999). "In situ thin-film texture determination." *Journal of Applied Physics* **85**(4): 2151 - 2156.

[35] Andrieu, S. (1996). "What information can be obtained by RHEED applied on polycrystalline films ?" *Surface Science* **360**(1 - 3): 289 - 296.

[36] Wang, H. Y. (2004). "Enhancement in ordering of FePt films by magnetic field annealing" *Applied Physics Letters* **85**(12): 2304 - 2306.

[37] Toney, M. F. (2003). "Thickness and growth temperature dependence of structure and magnetism in FePt thin films" *Journal of Applied Physics* **93**(12): 9902 - 9907.

[38] Stappert, S. (2003). "Gas-phase preparation of $L1_0$ ordered FePt nanoparticles" *Journal of Crystal Growth* **252**: 440 - 450.

[39] Dumestre, F. (2004). ”Superlattices of Iron Nanocubes Synthesized from $Fe[N(SiMe_3)_2]_2$ ” *Science* **303**(5659): 821 - 823.

[40] Acet M., Pepperhof W. (1961, Springer) ”Konstitution und Magnetismus des Eisens”

[41] Zakeri, K. (2006). ”Magnetic anisotropy of Fe/GaAs(001) ultrathin films investigated by in situ ferromagnetic resonance” *Journal of Magnetism and Magnetic Materials* **299**: L1 - L10.

[42] Meiklejohn (1956). ”New Magnetic Anisotropy.” *Physical Review* **102**(5): 1413 - 1414.

[43] R. Narkowicz, D. S. a. R. S. (2005). ”Planar microresonators for EPR experiments.” *Journal of Magnetic Resonance* **175**: 275 - 284.

[44] Zhang, Z. (1998). ”Ferromagnetic Resonance Force Microscopy on microscopic cobalt single layer films.” *Applied Physics Letters* **73**(14): 2036 - 2038.

[45] Durkan, C. (2002). ”Electronic spin detection in molecules using scanning-tunneling-microscopy-assisted electron-spin resonance.” *Applied Physics Letters 80*(3): 458 - 460.

[46] Wrachtrup, J. (1993). ”Optical detection of magnetic resonance in a single molecule.” *Nature* **363**: 244 - 245.

[47] Jaworski, M. (1997). ”Double stacked Dielectric Resonator for Sensitive EPR measurements.” *Journal of Magnetic Resonance* **124**(87 - 96).

[48] Sakamoto, Y. (1995). ”Design of a multicoupled loop-gap resonator used for pulsed-electron paramagnetic resonance measurements.” *IEEE Transactions on Microwave theory and techniques* **43**(8): 1840 - 1847.